

# Discriminating between individual-based models of collective cell motion in a benchmark flow geometry using standardised spatiotemporal patterns

Carine Beatrici,<sup>a,b</sup> Cássio Kirch,<sup>a</sup>, Silke Henkes,<sup>c</sup>, François Graner,<sup>b</sup> Leonardo Brunnet<sup>a</sup>

Collectively coordinated cell migration plays a role in tissue embryogenesis, cancer, homeostasis and healing. To study these processes, different cell-based modelling approaches have been developed, ranging from lattice-based cellular automata to lattice-free models that treat cells as point-like particles or extended detailed cell shape contours. In the spirit of what Osborne et al. [PLOS Computational Biology, (2017) **13**, 1-34] did for cellular tissue structure simulation models, we here compare five simulation models of collective cell migration, chosen to be representative in increasing order of included detail. They are Vicsek-Grégoire particles, Szabó-like particles, self-propelled Voronoi model, cellular Potts model, and multiparticle cells, where each model includes cell motility. We examine how these models compare when applied to the same biological problem, and what differences in behaviour are due to different model assumptions and abstractions. For that purpose, we use a benchmark that discriminates between complex material flow models, and that can be experimentally approached using cell cultures: the flow within a channel around a circular obstacle, that is, the geometry Stokes used in his historical 1851 experiment. For each model we explain how to best implement it; vary cell density, attraction force and alignment interaction; draw the resulting maps of velocity, density and deformation fields; and eventually discuss its respective advantages and limitations. We thus provide a recommendation on how to select a model to answer a given question, and we examine whether models of motile particles and motile cells display similar collective effects.

## 1 Introduction

Collectively coordinated cell migration plays a role in tissue embryogenesis, pattern formation, cancer, homeostasis, regeneration and healing<sup>1,2</sup>. It is a ubiquitous process involving different morphologies and mechanisms in different cell types and tissue environments<sup>3</sup>. Cells grow, move, divide or die, and also change size, shape or neighbours: all these processes contribute together to tissue shape and size changes<sup>4-6</sup> and generate stresses. Due to the cumulative effects of structural changes at subcellular and cellular levels, the tissue-scale response to these stresses is complex in terms of viscoelasticity<sup>7,8</sup>, yielding and jamming<sup>9,10</sup>.

Statistical physics and hydrodynamics approaches in active matter studies<sup>11-14</sup> have raised fundamental questions regarding symmetry breaking at the onset of cell migration, either in general<sup>2,15</sup> or in specific cases<sup>16,17</sup>. Other questions include motility-induced phase separation and its link to tissue glassiness<sup>18</sup>, and the onset of waves<sup>19</sup> or vortices<sup>20</sup>.

Individual-based numerical models of motile cells have been developed in several contexts, each one with its own variants, in two and/or three dimensions. Some models link the cell scale with

collective cell migration<sup>21</sup>, and a minority also include the sub-cellular scale<sup>22</sup>, pointing to cell motility and polarization as essential ingredients in tissue dynamics. Other models use the cell center as degree of freedom; in this case a cell is either treated as a point<sup>11,23,24</sup>, an elastic adhesive circle or sphere<sup>25-27</sup> or a polygon of a Voronoi tessellation<sup>9,28</sup>. Finally, some models describe the cell body in more detail, using the cell contour shape as degree of freedom. This includes descriptions based on vertices of polygons tiling the space<sup>29,30</sup>, pixels similar to experimental images (cellular Potts model)<sup>31-33</sup>, several vertices free to move and interacting pairwise<sup>34</sup>, or a smooth and continuous phase field<sup>35,36</sup>. Finally, some of these models are lattice-based while others are lattice-free.

An exhaustive list of commonly used models in literature is out of scope of this paper. In fact, “no one review paper can do justice to the entire field”, as claimed by a recent review<sup>22</sup>. In order to keep the computational cost reasonable, we have to perform choices. Our primary objective is to explore models covering the spectrum from entirely particle-like models to entirely cell-like ones. We thus leave the exploration of other important models, in particular the family of phase field ones, for future work.

Each of the models we consider here derives from existing non-motile cell simulation models reproducing tissue structure and simple dynamics. Several reviews exist, including those of Fletcher and coworkers<sup>37-39</sup>. The two-dimensional version of five models (cellular automaton, cellular Potts model, overlapping spheres, Voronoi tessellation, vertex model) have been compared, using a

<sup>a</sup> Instituto de Física, Universidade Federal do Rio Grande do Sul, Av. Bento Gonçalves 9500, C.P. 15051 - 91501-970 Porto Alegre, RS, Brazil

<sup>b</sup> Université Paris Cité, CNRS, Matière et Systèmes Complexes, F-75006 Paris, France.

<sup>c</sup> Leiden Institute of Physics, Leiden University, Niels Bohrweg 2, Leiden, NL-2333 CA, The Netherlands.

‡ Simulation codes are available at Stokes Flow Simulations.

common computational framework and four case studies<sup>37</sup>; the influence of cell proliferation, adhesion, death, differentiation and signaling range have been studied in detail, and practical conclusions are drawn regarding the choice of a model to address a given question.

In the context of cell tissues, the flow around a circular obstacle in a two-dimensional channel can play a significant role. This geometry favors shear and viscous flow, which is essential for understanding the heterogeneous deformation, deformation rate, and rearrangement rate of cells. These non-zero velocity gradients, resulting from the heterogeneity of cell velocity orientations, are critical for gathering the discriminant information regarding both amplitude and direction (so-called “tensor field” information) necessary for benchmarking cell migration models. Moreover, the flow around a circular obstacle was used in Stokes’ historical 1851 experiment<sup>40</sup> and is similar to the motion of an intruder within a cellular material<sup>10</sup>. For non-motile cellular materials like soap froth, this geometry has been particularly efficient in differentiating and testing different models’ predictions<sup>41</sup>. The corresponding experiment with cells is feasible and has been carried out several times<sup>7,42,43</sup>, as illustrated in Fig. 1. Quantitative comparison between experiments and models is beyond the scope of this study and will be the subject of future work.

Here, we build on these advances in simulation models and of benchmarking. In the spirit of Ref.<sup>37</sup>, we run comparable collective movement simulations in the Stokes geometry for five motile cell simulation models, chosen as representative of the progression from the simplest to the most detailed. The first model is derived from the now classical Vicsek and Grégoire particle models<sup>11,12</sup>. The second one, the Szabó-like particle model<sup>23</sup>, is similar, but dominated by cell velocity self-persistence instead of direct neighbor alignment. The third one, the self-propelled Voronoi model, is based on particles associated with a Voronoi tessellation<sup>9,28</sup>, is chosen because it is an intermediate between cell center and cell contour based models. The fourth one, derived from the cellular Potts model<sup>31,32</sup>, uses pixels and thus an experimental image can be directly compared with simulations (or even injected as the initial image of a simulation<sup>44</sup>). The last one, which uses multiparticle cells<sup>34</sup>, can handle highly deformed cells and the dissipation associated with cell shape changes. For all five models, and especially for the fifth, we have introduced new details with respect to the literature.

Our motivation is twofold. First, we want to understand how each model behaves, depending on its ingredients and underlying assumptions, and examine the common points and differences between models. In particular, models based on cell centers versus on cell contours display common properties (e.g. soft elastic particles versus self-propelled Voronoi<sup>45</sup>) but it is unclear to which extent. Second, we want to examine the respective advantages and limitations of each model: for each given scientific question we want to provide the reader with a guide to help choosing the most adequate model, the best implementation method and the range of parameter values. For that purpose, we vary input parameters such as cell density, attraction force and alignment interaction; as outputs we draw the resulting maps of velocity, density and deformation fields.

This paper is organized as follows. We first describe the common simulation set-up, the choice of parameters and measurements and present the formulation of the five models and their implementation. We then present the results for each model, that is the input parameter range and the output measurement maps. We compare and discuss these results, along with a guide for the reader (Table 15), and conclude.

## 1.1 Simulation set-up

Our benchmark is a standard simulation set-up common to the five models. Cells flow within a channel around a circular obstacle (Stokes geometry)<sup>41</sup>. To keep cells migrating and to emulate a steady-state-like regime, we constantly create new cells in the source region on the left side of the channel, in red on Fig. 2, and drop cells at the same rate in the sink region on the right side of the channel, in blue on Fig. 2 (with a few variations for the Voronoi model).

The cell diameter at equilibrium may depend on several model parameter values such as the force between neighboring cells, or the cell creation rate. In order to compare simulations, we use the cell equilibrium diameter as the unit length. In these units, the channel is 50 cells wide and the obstacle diameter is 15 cells while source and sink regions are only 1 cell long.

The simulations produce snapshots over which we make two very different sets of measurements, which we call “input measurements” and “output measurements”. Output measurements are our results, and are plotted as maps over the whole output measurement region, which is 75 cells long, and centers on the obstacle. Conversely, input measurements are used to monitor the simulation at the entrance of the output measurement region, and ensure the comparison between different models is performed in similar conditions. The input measurement region is 1 cell long and the spatial average is performed over the channel width.

Close to the source region, the creation process frequently produces transient artifacts which can vary from model to model, which motivates us to leave a model-dependent transition region between the source and the input measurement region. We set the obstacle center at least 100 cell diameters from the cell source region and we use the same distance from the obstacle center to the sink region. After a transient period to allow for the steady-state-like regime to establish itself, with a time scale determined by the typical cell velocity divided by the obstacle size, measurements are averaged in time over the simulation duration.

## 1.2 Acceptable parameter values

Each model has its own restrictions when it comes to acceptable parameter values. Our objective is to determine these values and identify the specific regions for each model where realistic cell flow can potentially occur.

We are interested in three main model parameters: alignment (that affects the collective migration), force/tension between neighbor cells (that affect the tissue liquid or solid behaviour) and cell creation rate (that affects the density). In Fig. 3, the eight limit cases are presented and identified by a number 0, 1, 2, ... 7 which we use throughout this article.

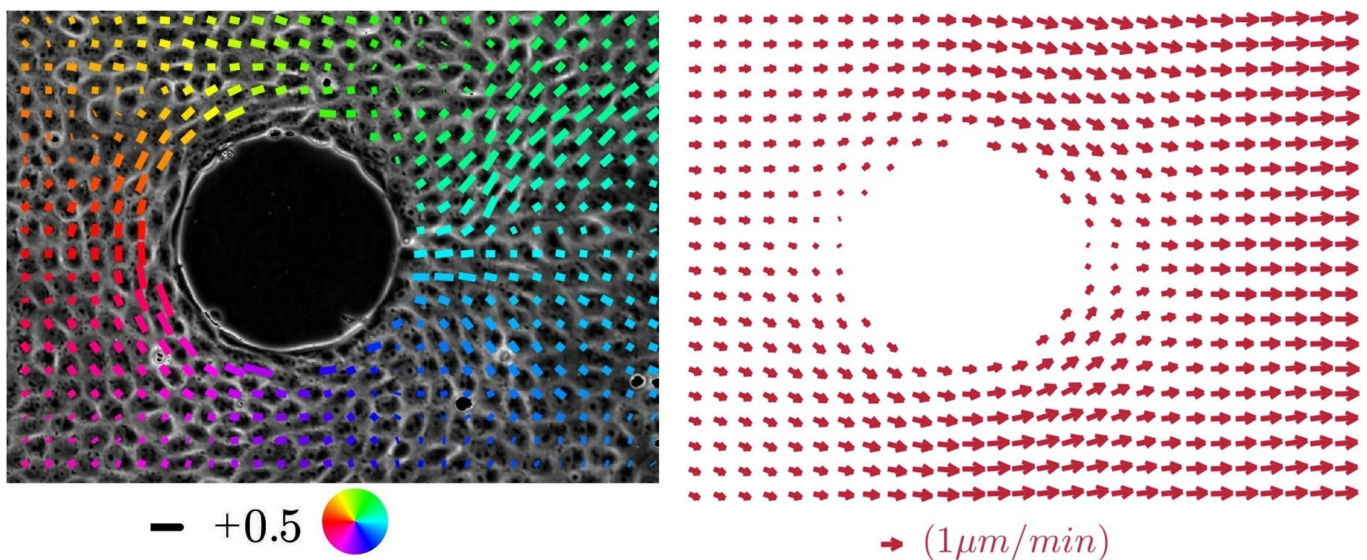


**Fig. 1** Experiment. A MDCK epithelial cell monolayer after 20 hours of migration in Stokes geometry, from left to right. On a flat substrate, a channel is drawn as a region where cells can adhere and crawl, while the channel walls and a circular obstacle are unfavorable for cell adhesion. (a) Deformation field measured for a phase contrast snapshot. The deformation tensor deviator is diagonalized and each bar represents its main axis of extension. The color codes for the angular position of each point, in polar coordinates originating at the obstacle center. (b) Corresponding velocity field averaged over 8 h. Scales are indicated below each panel. Maps are zoomed around the obstacle; actual strip length 4 mm, strip width 1 mm, obstacle diameter 0.2 mm, pixel size  $0.65 \mu\text{m}$ . Reproduced with permission from Ref.<sup>7</sup>, which did not publish the corresponding density field.

Some parameter limits are simply due to the numerical implementation, as the numerical solution may not converge, or the simulation may stop running due to infinite or non numerical values. Other more striking limitations are the physical and biological ones, like unrealistic densities or velocities. For example, the particles with Voronoi model can not support empty spaces; therefore for low densities, instead of creating empty spaces in the tissue the cells would stretch indefinitely. In many cases, some parameter values may generate artifacts in the dynamics and the physics is no longer correct.

### 1.3 Input measurements

#### 1.3.1 Implementation of input measurements.

A natural approach to compare simulations from different models would consist in standardizing the set of parameters from the different models in order to construct a common set of dimensionless numbers based on the model parameter values<sup>46</sup>. However, here, this approach is unfeasible: In fact, model ingredients are very diverse, especially since cell centers and cell contours are qualitatively different degrees of freedom. Even the number of model parameters varies a lot, from the parsimonious Vicsek-Grégoire model to the detailed Potts model, so that the number of relevant dimensionless parameters would be difficult to decide.

We have therefore chosen an alternative route: we define a standardized set of dimensionless *input measurements*. This has the following advantages: First, we can draw a common phase diagram, with identical axes corresponding to input measurements; we can then position each simulation on these axes, and thus on the same phase diagram. Second, if in the future a reader wants to compare the current five simulation models with a new one, it will not be

necessary to perform any theoretical analysis; it will be sufficient to measure the input quantities as we do here. Third, it will determine which models can or cannot be compared; if the input measurements do not present any intersection range, the models are too different to be comparable. Fourth, the input measurements are physical quantities and are in direct correspondence with the output measurements that we are interested in. In contrast, some model ingredients have no intuitive physical interpretation, or are not in correspondence with the output measurements. Fifth, the same approach will in principle be applicable to experiments too; in fact, the input measurements are accessible from experiments, as opposed to the dimensionless numbers based on the underlying parameter values.

Here, given our interests in the cellular and tissue aspects, we choose as input measurements three cell-scale characteristics: First, the *alignment* of a cell velocity with its neighbours velocity, which quantifies local order or disorder in the velocity field. Second, the *liquid or solid behaviour*, based on each cell center's local displacements relative to its neighbors. Third, the *relative density* that characterizes the confluence and compression of the monolayer, or its absence.

Additional measures, such as tissue softness and viscosity<sup>47</sup>, have been shown to provide valuable insights into cell behavior<sup>48,49</sup>. However, due to the variety of particle-based models (Vicsek, Szabó) and extended models (Voronoi, Potts, Multiparticle) utilized in our study, these measures cannot be readily applied to all models. Furthermore, as commented above, each model that we have used has additional parameters to vary beyond the three we have chosen, and these cannot be easily mapped to one another within each model. Therefore, we have selected the most common values reported in the literature for these fixed parameters. Below,

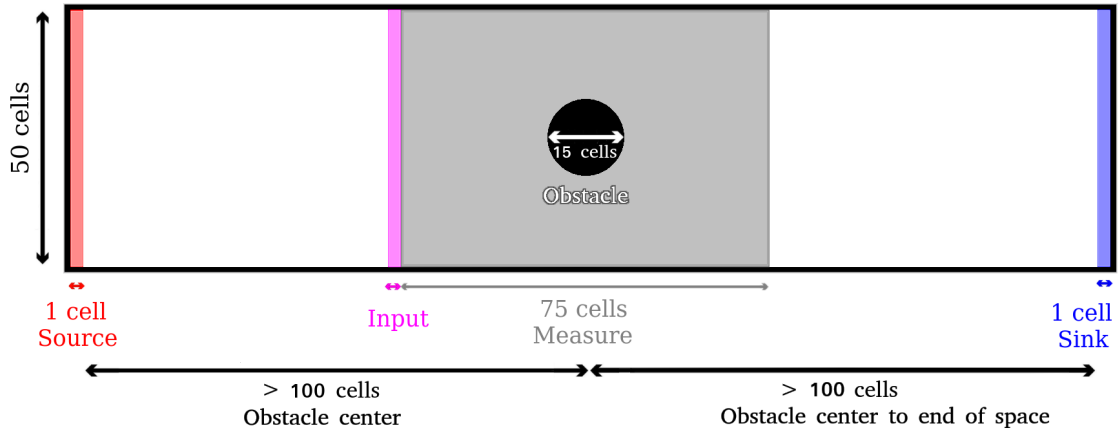


Fig. 2 Simulation set-up, definitions and dimensions (expressed in cell size units).

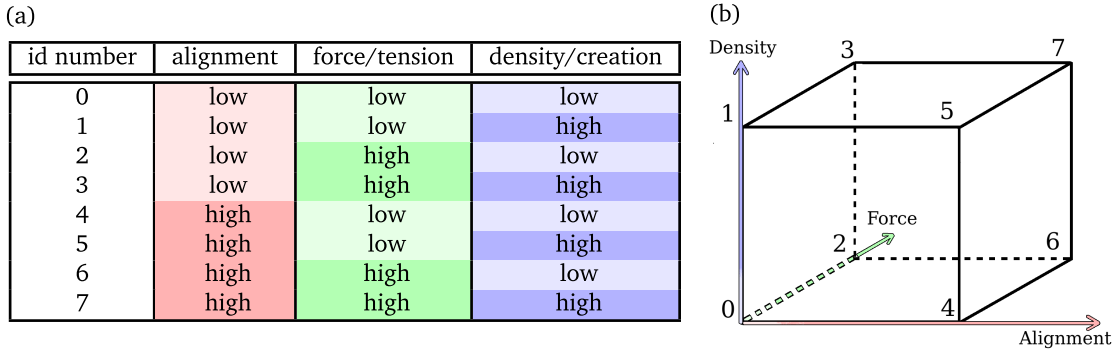


Fig. 3 Representations of parameter space. (a) The id numbers 0, 1, 2, ... 7, corresponding to the corners of a three-dimensional cube, identify the limits of parameters for the simulations and resulting maps. (b) Cube visualising extreme value labels, as defined in (a).

we examine each of the three chosen quantities in greater detail, and show how to measure them in practice.

For each model we determine the set of ingredients that can contribute to set these particular tissue characteristics; these ingredients are model-dependent. For instance, in some models the alignment is explicitly prescribed, while in others it is only an indirect consequence of ingredient choices. The cell behaviour can become more solid-like due to a large interaction force between cell centers, or to a large tension of cell-cell junctions. The density can directly or indirectly depend on several ingredients, for instance it increases with the cell creation rate (when it exists) and decreases with the free cell velocity.

We run simulations with several values of the model parameters to delimit the accessible range of input measurements. The phase diagram is three dimensional so that there are eight combinations of limit cases which we explore (Fig. 3). Note that in principle, there can be several combinations of model parameter values that result in the same limit case. Exploring these combinations of parameter values is beyond the scope of this work. Here, we choose to change as few parameter values as possible at a time, ideally one.

### 1.3.2 Choice of dimensionless input measurements.

To measure the degree of alignment of motile cell movements, we use the parameter originally proposed by Vicsek *et al.*<sup>11</sup>, the veloc-

ity order parameter:

$$\phi = \frac{1}{N} \sum_{i \in N} \frac{\vec{v}_i}{|v_i|} \quad (1)$$

where  $N$  is the number of cells and  $\vec{v}_i$  is the velocity of cell  $i$ . If each cell movement direction is uncorrelated with the surrounding ones,  $\phi = 0$ , cells form a non-collective flow. Conversely, if cells are all moving in the same direction,  $\phi = 1$ , they form a collective flow.

In order to evaluate the level of solidity or liquidity in the tissue, we could employ a measure commonly used in the soft matter field: the mean-square displacement (*MSD*). This measure quantifies the distance that a particle travels in time  $t$ , and is averaged spatiotemporally, i.e., over both space and time, denoted as  $\langle (\mathbf{r}(t_0 + t) - \mathbf{r}(t_0))^2 \rangle_{t_0, \text{space}}$ . When *MSD* reaches a value around  $\sigma^2$ , where  $\sigma$  represents the typical size of cells, it indicates the occurrence of a glass-to-liquid transition. Nevertheless, this measure is only an indirect indicator of rearrangements, and it is sensitive to spatial irregularities and the method of overall flow subtraction.

We thus choose here to use the more robust parameter proposed by Grégoire *et al.*<sup>12</sup>:

$$\Delta = 1 - \frac{1}{n_i} \sum_{i \sim j} \left( 1 - \frac{r_{ij}^2(t)}{r_{ij}^2(t+T)} \right) \quad (2)$$

where  $r_{ij}(t)$  is the distance between centers of cells  $i$  and  $j$  at time  $t$ , while  $r_{ij}(t+T)$  is their distance after time interval  $T$ . This sum

is normalized by the number of particles  $n_i$ . By that definition  $\Delta$  is close to one when a cell's motion is only fluctuating locally, keeping most of its neighborhood: this is solid-like behaviour. Conversely,  $\Delta$  is close to zero when a cell frequently exchanges most of its neighborhood: this is liquid-like behaviour. The value of  $\Delta$  of course depends on the choice of  $T$ , and this point is even more sensitive for an out-of-equilibrium tissue like the one we consider here. To choose  $T$ , we use an adaptive method: We first run the transient simulation time steps, and list the cells inside the input measurement region. We then track them while they flow over one obstacle radius and calculate  $\Delta$  during this time interval  $T$ . Using the measurement over an interval of one obstacle radius just beyond the region of input measurements allows us to define whether the cells exchange their neighborhood along a spatially well-defined region, sufficiently far from the source and the obstacle, and independent of the velocity associated with the flow.

In order to convert the density into a non-dimensional form, we define

$$\delta\rho = \left\langle \frac{\rho}{\rho_{eq}} \right\rangle - 1, \quad (3)$$

where  $\rho$  denotes the number of cells per unit area, and  $\rho_{eq}$  represents its equilibrium value under model-specific conditions, i.e., in the absence of external forces and stresses. According to this definition,  $\delta\rho$  vanishes when, on average, the cells are at equilibrium density. It becomes positive when the cells are compressed, and negative when the cells are stretched or create gaps.

#### 1.4 Output measurements

Output measurements are performed over 466 boxes disposed in a  $28 \times 18$  rectangular grid (minus 38 grid elements corresponding to the obstacle). We measure and represent the following three quantities.

The normalized density  $\delta\rho = 0$  is the same as the one used as an input measurement (Eq. 3). It is a scalar quantity and is represented by a color. Blue represents negative values of  $\delta\rho$ , i.e. density lower than the equilibrium; white represents  $\delta\rho = 0$ , i.e. density at equilibrium; and red represents positive values of  $\delta\rho$ , i.e. density higher than in equilibrium.

For each snapshot, we measure each cell velocity during the time interval immediately following the snapshot. The velocity, averaged over all cells in the box, is a vector represented as an arrow which we place in the middle of the box, while a yellow unit scale arrow is shown in the middle of the obstacle. In the snapshot, we color each particle by its direction of movement according to the angular color map shown in Fig. 4.

The deformation is the anisotropy of the coarse-grained cell shape deformation (not to be confused with the coarse-grained average of the cell shape deformation anisotropy). It is measured by averaging links between cells using the inter-cellular texture matrix as defined in reference<sup>50</sup>. We divide the system into boxes of four cell diameters in size and perform a time average of the textures over typically 50 snapshots, during which cells have moved at least 30 cell diameters. The average texture is diagonalized yielding two eigenvalues,  $L_{max}^2$  and  $L_{min}^2$ . From these we calculate the cell deformation deviator amplitude,  $\frac{1}{2} \ln \frac{L_{max}}{L_{min}}$ , and the cell

deformation deviator orientation, which is the angle of the larger eigenvalue direction relative to the  $x$ -axis<sup>51</sup>. We represent the deviator as a bar, with a length corresponding to the magnitude of the deformation anisotropy and with an angle corresponding to its major axis. To indicate scale, the red line in the middle of the obstacle represents a deformation of  $\ln 2$ , corresponding to cells whose length is twice their width.

## 2 Materials and Methods: Simulation Models

In this section we present the simulation models covering their principle, their implementation, and their parameters. Ingredients include motility, alignment, polarization, interaction (force between cell centers, or cell-cell junction tension), area, perimeter, density, cell creation and cell destruction. We emphasize that all models are in their motile version.

For each model, we determine three model parameters that affect the three input measurements alignment (Eq. 1), rigidity (Eq. 2) and density relative to the equilibrium density (Eq. 3). We vary these three model parameters (keeping the others fixed) and determine the range of their values which lead to low and high levels of these input measurements. We also briefly discuss the effects on running simulations outside of this parameter range.

### 2.1 Vicsek model

The Vicsek model<sup>11</sup> describes each cell  $i$  as a single motile particle. For each time step, the particle position evolution is given by

$$\vec{x}_i(t + \Delta t) = \vec{x}_i(t) + \vec{v}_i(t)\Delta t. \quad (4)$$

Here, the time interval is fixed as 1 and the time scale is determined by the velocity module, chosen as  $v_0 = |\vec{v}_i| = 0.05$ . Each particle has a speed of fixed modulus, so it always moves regardless of the external forces and all particles are identical.

The sole degree of freedom is the velocity direction, which evolves according to<sup>12</sup>:

$$\theta_i(t + \Delta t) = \arg \left[ \sum_{j \sim (i)} \alpha \frac{\vec{v}_j(t)}{v_1} + \sum_{j \sim (i)} \beta \vec{f}_{i,j}(t) + \eta \vec{u}_i(t) \right] \quad (5)$$

The first term is the alignment with neighbors, here an explicit model ingredient. These neighbors are defined according to a metric (i.e. distance-based, as opposed to topology-based) criterion where  $j$  is neighbour to  $i$  if their distance is smaller than a distance  $r_{max} = 1$ . The collective migration behaviour is then tuned by the coupling parameter  $\alpha$ .

The second term is the pairwise, radial force between neighboring particles, tuned by the  $\beta$  coupling parameter:

$$f_{i,j} = \begin{cases} 0 & r_{ij} \geq r_{max} \\ 1 - \frac{r_{ij}}{r_{eq}} & r_c < r_{ij} < r_{max} \\ +\infty & r_{ij} \leq r_c \end{cases} \quad (6)$$

Particles have a hard-core repulsion ( $f_c = 1000$ ) of below a radius  $r_c = 0.18$ . Between  $r_c$  and  $r_{max}$  the force is harmonic and the equilibrium force distance is  $r_{eq} = 0.8$ ;  $r_{eq}/2$  is used as the size unit. This equilibrium distance we define as the equilibrium density for  $\rho_{eq} = 1/(\pi(r_{eq}/2)^2)$ . The last term is the vector noise where  $\vec{u}_i(t)$  is

a random unitary vector, and where we keep the amplitude  $\eta$  fixed as one.

The system dimensions in simulation units are: channel length 101, width 25, obstacle center position (50, 12.5), obstacle radius 3.75, source region from  $x = 0$  to 1, sink region at  $x = 100$ . The time scale is given by the particle speed and time interval; we keep  $v_0\Delta t < 0.1 r_C$  to prevent a particle from jumping over another one.

Parameter	Level	Value
Alignment ( $\alpha$ )	low	0.0
Alignment ( $\alpha$ )	high	0.5
Force ( $\beta$ )	low	2.0
Force ( $\beta$ )	high	5.0
Creation (rate)	low	0.007 to 3.0
Creation (rate)	high	0.0105 to 5.0

**Table 1** Limit values for the parameters varied in the Vicsek model. The particle creation rate needs to be carefully adjusted in order to keep the flow as confluent and steady as possible, and this adjustment strongly depends on the alignment degree. The lowest creation rate to keep confluent flow is 0.007 for disordered cells, while it is 3.0 to keep a highly aligned confluent flow. In order to produce a high density flow, we increase creation rate by approximately 50%, which leads to the high creation rate of 0.0105 for disordered cells and 5 for ordered cells.

id	$\phi$	$\Delta$	$\delta\rho$
0	0.124	0.025	0.711
1	0.122	0.018	1.022
2	0.158	0.686	0.062
3	0.154	0.623	0.381
4	0.967	0.824	0.174
5	0.990	0.892	0.997
6	0.963	0.908	0.169
7	0.988	0.933	1.014

**Table 2** Input measurements for the Vicsek model. The values of the three input measurements, alignment  $\phi$ , liquid-solid behaviour  $\Delta$  and normalized density  $\delta\rho$ , are indicated for the Vicsek model simulations with different values of the three model parameters. A lighter color means the simulation was performed with a lower level of the parameter related to that measure, a darker color means a higher level of that parameter, see Table 1. For example, the line with id = 3 is the result of a simulation with low alignment, high force and high creation rate.

Fig. 4 shows simulation snapshots in the limit cases. The three model parameters directly affect the input measurements, as shown in Table 2. First, a low value of the alignment  $\alpha$  prevents any collective behaviour (see top row of Fig. 4), i.e the  $\phi$  value is low. When the alignment  $\alpha$  value is high, the collective phase is well simulated, and the  $\phi$  value is high. Note that at high alignment, particles barely separate and  $\Delta$  is high, as in a solid phase. Second, the force  $\beta$  determines the liquid versus solid behaviour,  $\Delta = 0$  to 1; note the nearly crystalline structure in images 2 and 3 of Fig. 4. Finally, the density  $\delta\rho$  increases with the cell creation rate. A low creation rate keeps the density around confluence while a high one keeps the cells under pressure. This creation rate needs to be carefully adjusted in order to keep the flow as steady as possible (Table 1). Note the frequent formation of voids at different parameter values. Overall, the Vicsek model is robust to parameter variation and artifacts are easy to avoid.

## 2.2 Szabó model

The Szabó model<sup>23</sup> is also based on motile particles, but is defined as a set of continuous differential equations, and with no explicit neighbor alignment term. Each cell has a polarity direction, which determines self-persistence of the velocity. This polarity changes with collisions and with an angular noise. Any collective behavior in this model is a result of this self-persistence<sup>52,53</sup>.

The  $i$ -th particle polarity  $\hat{n}_i$  is a unitary vector with direction  $\theta_i$ . This angle tends to relax to the direction of the particle displacement  $\vec{v}_i = d\vec{r}_i/dt$  in a characteristic time  $\tau$ :

$$\frac{d\theta_i(t)}{dt} = \frac{1}{\tau} \arcsin \left[ \left( \hat{n}_i \times \frac{\vec{v}_i}{|\vec{v}_i|} \right) \cdot \hat{e}_z \right] + \xi_i \quad (7)$$

The angular noise  $\xi_i$  follows a Gaussian distribution with zero mean  $\langle \xi(t) \rangle = 0$  and auto-correlation  $\langle \xi(t) \xi(t') \rangle = \frac{\eta^2}{12} \delta(t, t')$  where  $\delta$  is the Dirac delta function. There is no direct noise on the displacement, and the angular noise only changes the polarization direction;  $\hat{e}_z$  is the unit vector orthogonal to the plane of motion.

The velocity evolution of the  $i$ -th particle is given by

$$\frac{d\vec{r}_i(t)}{dt} = v_0 \hat{n}_i(t) + \mu \sum_{j=1}^N \vec{f}(|\vec{r}_{ij}|). \quad (8)$$

Without any external influences, the particle will move in the polarity direction with its free velocity  $v_0$ . The interaction with particles or obstacles follows an overdamped Langevin dynamics, where the mobility (or inverse friction)  $\mu$  controls the amplitude of the velocity response to forces. Additionally, if force and polarity vectors are aligned, particle velocity increases while it slows down in the converse case. This type of non-reciprocal interaction is responsible for the global flocking state in the system.

The force between two particles  $i$  and  $j$  is radial, i.e. it only depends on their distance  $r_{ij} = |\vec{r}_{ij}|$ :

$$f(r_{ij}) = \begin{cases} F_{\text{rep}} \frac{r_{ij} - r_{\text{eq}}}{r_{\text{eq}}} & r_{ij} < r_{\text{eq}} \\ F_{\text{adh}} \frac{r_{ij} - r_{\text{eq}}}{r_{\text{max}} - r_{\text{eq}}} & r_{\text{eq}} \leq r_{ij} < r_{\text{max}} \\ 0 & r_{ij} \geq r_{\text{max}} \end{cases} \quad (9)$$

At short distance the particles repel each other with a harmonic repulsion with stiffness parameter  $F_{\text{rep}}$ . If the particles are more distant than the equilibrium distance  $r_{\text{eq}}$  they adhere with adhesion parameter  $F_{\text{adh}}$ , and finally, if the particles are more distant than  $r_{\text{max}}$  they do not interact.

The fixed parameters are: interaction coupling  $\mu = 1.0$ , repulsion between particles  $F_{\text{rep}} = 30.0$ , particle free velocity  $v_0 = 0.05$ , noise amplitude  $\eta = 1.0$ . The interaction of the obstacle with the particles is defined as a central repulsive force with stiffness constant equal to 100.0. The maximum interaction and alignment distance is  $r_{\text{max}} = 1.0$ , and the equilibrium force distance is  $r_{\text{eq}} = 0.666$ . To avoid crystallization as an artifact of this model we introduce in the equilibrium distance  $r_{\text{eq}}$  a polydispersity 0.1.

The system dimensions in simulation units are channel length 101, width 25, obstacle center position (50, 12.5), obstacle radius 3.75, source region from  $x = 0$  to 1, and sink region at  $x = 100$ . The time interval used for numerical integration is  $\Delta t = 0.005$ , chosen for numerical stability and also such that  $\Delta t \ll \tau$ .

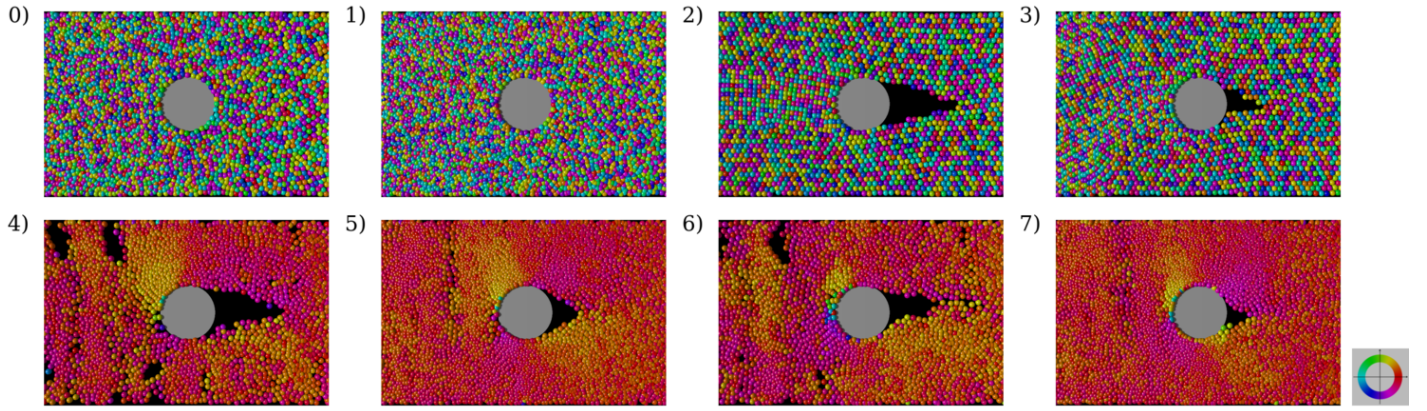


**Fig. 4** Snapshots for the motile cell simulation in the Stokes geometry in the Vicsek model's eight limit cases where the panel labels correspond to Fig. 3. The values for the parameters used in this model are specified in Table 1. Images with even numbers present systems with density close to confluence, while the odd ones are constructed with higher densities. The top row presents the low alignment cases while the bottom one presents the high alignment ones. The four images on the left correspond to low attraction forces (liquid-like), while the four images on the right correspond to high attraction forces (solid-like). The images are restricted to an area around the obstacle; particle source and sink regions are not depicted. The color of each particle is related to the direction of its movement, see the orientational color map at the bottom right. Objects migrating in the flow direction, along the positive  $x$ -axis towards the right, are displayed in red. Objects moving upwards, along the positive  $y$ -axis, are represented in yellowish-green. Objects moving backwards, towards the left, are cyan. Objects moving downwards are a blueish-purple color. A black background color corresponds to holes in the tissue.

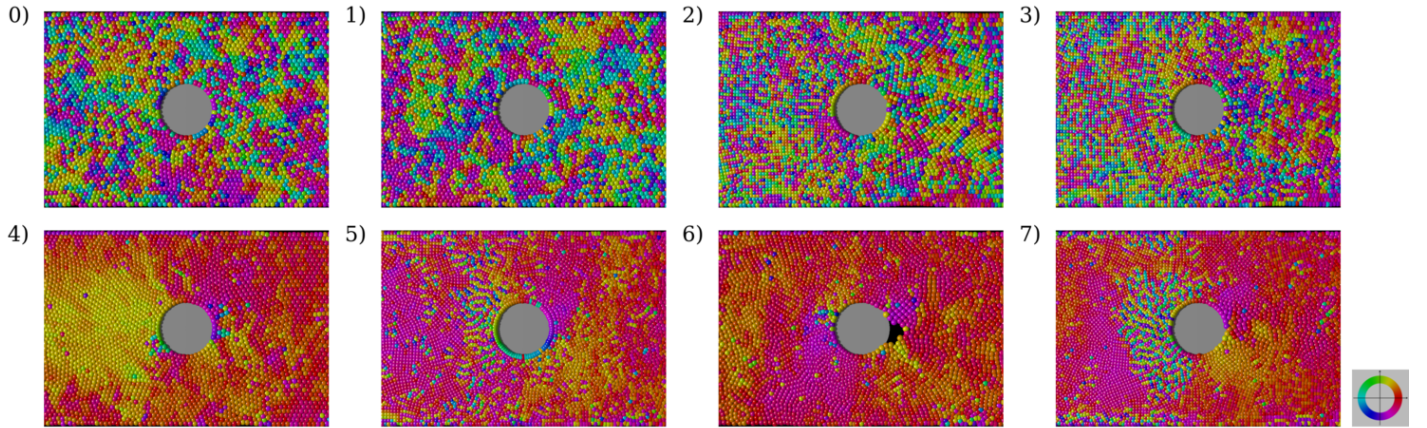


**Fig. 5** Snapshots for the Szabó's eight limit cases; same caption as Fig. 4. See Table 3 for parameter values.

Fig. 5 shows simulation snapshots in limit cases. Table 3 shows which parameters we vary. First, the relaxation time  $\tau$ , where low values of  $\tau$  favor global alignment. The relation between  $\tau$  and alignment is indirect, and not explicit; note for instance that the simulation time interval limits the maximum possible alignment. Second, the adhesion parameter  $F_{\text{adh}}$ : a high value of  $F_{\text{adh}}$  favors solid-like behaviour, but it also affects the density and should remain small enough to avoid particle overlap. Third, the creation rate: it has to be carefully tuned in order to keep a constant density. Note that void formation is rare in this model. Velocity coherence regions are wider than for the Vicsek model, and the disordered region before the obstacle appears at higher densities (labels 5 and 7). Here again, at high alignment, particles barely separate and  $\Delta$  is high, as in a solid phase.

### 2.3 Voronoi model

In a Voronoi model, the degree of freedom is the cell center, but cells have geometrical quantities (a shape, a perimeter, an area, vertices, edges) which can play a role in the dynamics. The neighbours are defined by the Delaunay triangulation (the dual of the Voronoi tessellation).

We use here the self-propelled particle version of the Voronoi model proposed by Bi *et al.*<sup>9</sup> and implemented with boundaries and division by Barton *et al.*<sup>28,54</sup>. As in the Szabó model, the  $i$ -th Voronoi velocity is given by an overdamped Langevin equation:

$$\frac{d\vec{r}_i}{dt} = v_0 \hat{n}_i - \mu \nabla_{\vec{r}_i} E \quad (10)$$

where  $v_0$  is the free particle velocity and  $\hat{n}_i$  the particle polarity while  $\mu$  is the mobility. The last term,  $\vec{F}_i = -\nabla_{\vec{r}_i} E$ , is the force term acting on particle  $i$ . It is written in terms of the energy  $E$  calculated

Parameter	Level	Value
Alignment ( $\tau$ )	low	100.0
Alignment ( $\tau$ )	high	0.1
Force ( $F_{adh}$ )	low	1.0
Force ( $F_{adh}$ )	high	3.0
Creation ( $div$ )	low	0.01 to 0.35
Creation ( $div$ )	high	0.015 to 0.525

**Table 3** Limit values for the parameters varied in the Szabó model. The creation rate needs to be carefully adjusted in order to keep the flow as confluent and steady as possible, and this adjustment strongly depends on the degree of alignment: The lowest creation rate to keep confluent flow is 0.01 for disordered cells, while it is 0.35 to keep a highly aligned confluent flow. In order to produce a high density flow, we increase creation rate by approximately 50%, which leads to the high creation rate of 0.015 for disordered cells and 0.525 for ordered cells.

id	$\phi$	$\Delta$	$\delta\rho$
0	0.252	0.171	0.153
1	0.250	0.226	0.275
2	0.195	0.914	0.801
3	0.241	0.944	1.037
4	0.969	0.912	0.194
5	0.845	0.723	0.936
6	0.953	0.813	0.173
7	0.939	0.776	0.885

**Table 4** Input measurements for the Szabó model. A lighter color means the simulation was performed with a lower level of the parameter related to that measure, a darker color means a higher level of that parameter, see Table 3.

for the entire Voronoi tiling, which includes the interaction with neighbors through a preferred area and perimeter:

$$E = \frac{K}{2} \sum_i (A_i - A_i^0)^2 + \frac{\Gamma}{2} \sum_i P_i^2 + \sum_{ij} \Lambda_{ij} \quad (11)$$

Here, the preferred area is  $A_i^0$  and each cell's actual area  $A_i$  is determined by its Voronoi tile. The compressibility modulus  $K$  determines the effect of area variation on energy;  $\Gamma$  plays the same role for the perimeter  $P_i$ , whose preferred value  $P^0 = -\Lambda/\Gamma$  is implicit in the last term of the energy. The latter is summed over each cell-cell junction  $ij$ , which is a Voronoi edge, and  $\Lambda$  is its tension.

The model can incorporate both an explicit neighbor alignment and the self-persistence of a polarity, with an angular noise, so that the cell polarity evolves according to

$$\frac{d\hat{n}_i}{dt} = \vec{\tau}_i + \vec{\xi}_i \quad (12)$$

where the torque  $\vec{\tau}_i$  acting on the particle is given by

$$\vec{\tau}_i = -\hat{n}_i \times \nabla_{\hat{n}_i} E_{align} \quad (13)$$

We separately test both options (Table 5). If  $E_{align}$  is result of the explicit neighbor alignment, similar to the Vicsek particle model, then  $E_{align} = -J \sum_j \hat{n}_i \cdot \hat{n}_j$  and in that case  $J$  is the alignment parameter. If  $E_{align}$  is result of the particle self persistence, similar to the Szabó model, then  $E_{align} = -\frac{1}{\tau} \hat{n}_i \cdot \hat{v}_i$  in which case  $\tau$  is the alignment parameter.

The second variable parameter is the cell-cell junction tension  $\Lambda$ , uniform for all cells and independent of the junction length. This measure maps to the shape parameter  $p_0 = -\frac{\Lambda}{\Gamma\sqrt{A_0}}$  that controls the mechanical transition from a rigid to a floppy system in this model<sup>9</sup>. The third parameter is the initial density,  $\rho_0$ . Note that in this model, we create new particles by division: cells inside the source region divide every 100 time steps with a probability of 3%. When we increase the cell density in the source area, the rate of creation is indirectly increased. Also, we do not destroy the cells at the end of the channel as this is difficult to integrate into a persistent Delaunay triangulation, so we simply leave enough free space for the particles to migrate.

Parameter	Level	Value
Alignment ( $J$ )	low	0.0
Alignment ( $J$ )	high	0.5
Alignment ( $\tau$ )	low	500.0
Alignment ( $\tau$ )	high	0.5
Force ( $\Lambda$ )	low	-4.0
Force ( $\Lambda$ )	high	-4.5
Creation ( $\rho_0$ )	low	1.0
Creation ( $\rho_0$ )	high	1.5

**Table 5** Limit values for the parameters varied in the Voronoi model. Note the two options for alignment: either  $J$  (for neighbours) or  $\tau$  (for persistence).

The system dimensions in simulation units are: channel length 200, width 50, obstacle center position (0, 0), obstacle radius 7.5, channel left at  $x = -100$ , channel right at  $x = 100$ . Each cell has an equilibrium area  $A_i^0 = \pi$ , and stiffness  $K = 1$ ,  $\Gamma = 1$  as well as  $\mu = 1$ ,  $v_0 = 0.6$  and a rotational noise amplitude  $\xi_i(t) \cdot \xi_j(t') = 2D_r \delta_{ij} \delta(t - t')$  with  $2D_r = 0.5$ .

id	$\phi$	$\Delta$	$\delta\rho$
0	0.182	0.373	0.619
1	0.155	0.011	0.901
2	0.205	0.624	0.806
3	0.173	0.061	1.042
J0	0.582	0.661	0.393
J1	0.623	0.666	1.031
J2	0.942	0.509	0.507
J3	0.903	0.718	0.560
$\tau$ 0	0.862	0.736	0.621
$\tau$ 1	0.501	0.099	1.171
$\tau$ 2	0.903	0.794	0.617
$\tau$ 3	0.851	0.544	1.114

**Table 6** Input measurements for the Voronoi model. A lighter color means the simulation was performed with a lower level of the parameter related to that measure, a darker color means a higher level of that parameter, see Table 5.

Fig. 6 shows simulation snapshots in the limit cases, see Table 6. As expected, a low tension favors a liquid behaviour and a high tension favors a solid one. But the density also plays a strong role: high density favors Voronoi topological changes, so that  $\Delta$  value is low as in a liquid phase. The neighbor alignment is difficult to tune: when we increase the parameter  $J$ , before the system reaches a collective behaviour some artifacts appear. Examples



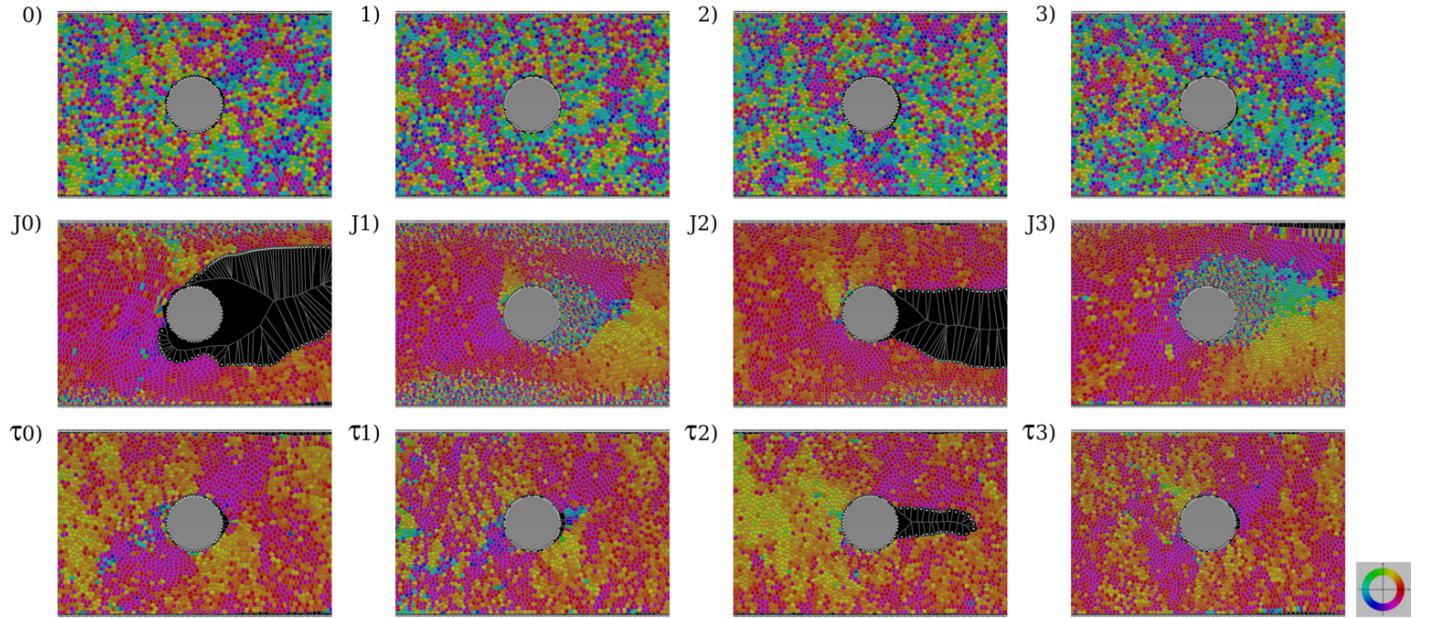


**Fig. 6** Snapshots for the Voronoi model limit cases. The obstacle and the walls are groups of fixed particles represented by small white particles. Clinging particles are also represented this way. Moving particles' color indicate their velocity direction according to the color scheme at the bottom right. The numbers indicate the levels of each parameter, see Tables 3a and 5. The first line corresponds to the case without neighbor alignment and low self-persistence. The second line is for high explicit neighbor alignment, while the third line imposes high self-persistence. Images with even numbers present systems with density close to confluence, while the odd ones are constructed with higher densities. The six images on the left of the figure correspond to low cell-cell junction tension, while the six on the right correspond to high junction tension.

include the empty spaces after the obstacle when density is low (images J0 and J2), disordered regions after the obstacle when density is high (images J1 and J3), or particle accumulations (top left of image J3). Conversely, the alignment obtained with high self-persistence (bottom row, indicated by the letter  $\tau$ ) yields more realistic collective behaviours, consistent with the observation of a flocking Voronoi model phase with self-alignment in Refs.<sup>55,56</sup>.

## 2.4 Potts model

In its version without motility<sup>57-59</sup>, the cellular Potts model represents each cell as a connected set of pixels on a square lattice, like a picture of experimental cells. The degrees of freedom are the cell contours, and each cell has a preferred area. The evolution of the pattern is described by the following Monte-Carlo dynamics. At each step, we choose at random a pixel of cell  $i$ . If it is in the bulk of the cell, it is not examined. If it is near the cell contour, we propose to switch its value by copying that of a neighboring pixel, in another cell  $j$ . The energy cost  $\Delta H$  (where  $H$  is the total system energy) that this copy incurs is evaluated. If the energy  $H$  of the system would decrease with the proposed copy, then it is always accepted (which is equivalent to moving the junction between  $i$  and  $j$  by one pixel). If the energy would instead increase, the proposed copy will be accepted with a probability that exponentially depends on the cost  $\Delta H$  and on a fluctuation allowance,  $\beta$ :

$$P = \begin{cases} e^{-\beta\Delta H} & ; \Delta H > 0 \\ 1 & ; \Delta H \leq 0 \end{cases} \quad (14)$$

In this case without any cell motility, the energy is given by

$$H = \sum_{i \sim j} J + \lambda_A \sum_i (A_i - A_0)^2, \quad (15)$$

where the first term is the tension of the junction between cells  $i$  and  $j$ , and the sum is performed over all pixels at the junction, hence encompasses the junction length. As  $J$  increases, changes are less probable, and the tissue has a more solid-like behaviour. The second term is the area conservation: the cell has an equilibrium area  $A_0$  and an actual area  $A_i$ , while the parameter  $\lambda_A$  is an area compressibility modulus. When there is a free space between cells, it is treated as a zone with no preferred area and no compression modulus, and its border with a cell has tension  $J$ . The channel walls and the obstacle are treated as a fixed zone without changes.

In the present work, we add motility to the Potts model based on Käfer *et al.*<sup>31</sup> cells by introducing the following motile force  $\vec{F}$ :

$$\Delta H = \vec{F}_i \cdot \vec{c}(i, j), \quad (16)$$

where  $\vec{c}$  is the copy vector. That is, for each pixel copy proposed during the Monte-Carlo step, the vector  $\vec{c}$  which links both pixels is a proxy of the direction of movement for the whole cell. If the copy is aligned with the force, the energy decreases and the copy is favored; conversely, if the copy vector has a direction opposed to the force, the energy increases and the copy is less probable. If the copy is perpendicular, it does not change the energy: hence some random perpendicular copies occur.

The motile force is:

$$\vec{F}_i(t + \Delta t) = \alpha \hat{P}_i(t) \quad (17)$$

Here  $\alpha$  is the total motility parameter; if it is zero the cell has no motility and  $\vec{v}_i$  is the past cell velocity before the change. The cell polarity is defined as the direction of the motile force, and thus of  $\vec{c}(i, j)$ . Both neighbor alignment and self-persistence terms can be implemented as:

$$\hat{P}_i(t + \Delta t) = \left[ \lambda_C \sum_{j \sim i} \hat{P}_j(t) + \lambda_P \hat{v}_i(t) \right]. \quad (18)$$

We have observed that, since  $\vec{c}(i, j)$  is pixelated, it yields highly fluctuating simulations. We thus mostly study the neighbor alignment term, by making  $\lambda_C$  variable. The second variable parameter is  $J$ , i.e. the tension of cell-cell junctions. The third parameter is the division area  $A^*$ . In the source region, the mother cells grow, and once they reach  $A^*$  they divide into two particles. To obtain higher density values we decrease  $A^*$  (Table 7), and other parameters are fixed.

Parameter	Level	Value
Alignment ( $\lambda_C$ )	low	0.0
Alignment ( $\lambda_C$ )	high	5.0
Force ( $J$ )	low	50
Force ( $J$ )	high	150
Creation ( $A^*$ )	low	80
Creation ( $A^*$ )	high	53.33

**Table 7** Limit values for the parameters varied in the Potts model. Note that bigger area  $A^*$  means less divisions.

All dimensions are expressed in pixels: channel length 2020, width 520, obstacle center position (810,260), obstacle radius 74, cell target area  $A_0 = 100$ . We use  $\alpha = 100$  and  $\beta = 1/50$ ,  $\lambda_A = 10$ ,  $\lambda_P = 1$ .

id	$\phi$	$\Delta$	$\delta\rho$
0	0.101	0.090	0.224
1	0.084	0.099	0.654
2	0.100	0.777	0.282
3	0.089	0.822	0.797
4	0.498	0.772	0.187
5	0.460	0.613	1.114
6	0.485	0.791	0.058
7	0.570	0.811	1.114

**Table 8** Input measurements for the Potts model. A lighter color means the simulation was performed with a lower level of the parameter related to that measure, a darker color means a higher level of that parameter, see Table 7.

Fig. 7 shows simulation snapshots in limit cases, see Table 8. While voids between cells are possible to simulate, here we do not intend to simulate them so by construction there are none. Note that the polarization is nearly random in the top images where there is no collective motion. When in collective motion, the polarization is overall aligned, with direction fluctuations only close to the obstacle.

## 2.5 Multiparticle model

In this work we introduce a Multiparticle model where several vertices are free to move and interacting pairwise, in the same spirit as Refs.<sup>34,60</sup>.

Each cell is composed of two kinds of motile particles: a central one and several peripheral ones (Fig. 8). The central one (representing the nucleus), also labelled  $\mu$ , interacts only with the peripheral particles of the same cell (representing the membrane or the cytoskeleton), which are labelled  $\mu, i$ .

Within a given cell the neighborhood is fixed. Each peripheral particle is always a neighbor to the central particle, and to two other peripheral particles. In addition, the peripheral particles of one cell are capable of interacting with the peripheral ones from neighboring cells and so are responsible for cell-cell interactions. We use the following notations:  $v^\mu$  is the speed of the central particle of cell  $\mu$ ;  $v_i^\mu$  is the speed of the peripheral particle  $i$  of cell  $\mu$ ; when two particles are neighbors we note  $i \sim j$ , finally  $\vec{r}_{i,j}^{\mu,\nu}$  is the vector connecting the position of particle  $i$  from cell  $\mu$  to the position of particle  $j$  from cell  $\nu$ .

An individual particle is described by an adapted Vicsek equation and the central particle movement of the  $\mu$ -th cell is given by:

$$\vec{x}^\mu(t + \Delta t) = \vec{x}^\mu(t) + \vec{v}^\mu(t)\Delta t. \quad (19)$$

As in the Vicsek model, the velocity has a constant modulus  $|\vec{v}^\mu|$ . Its direction depends on the alignment and forces of the peripheral particles of the same cell. The velocity direction  $\theta^\mu$  of the central particle evolves according to

$$\theta^\mu(t + \Delta t) = \arg \left[ \alpha \sum_{i \in \mu} \vec{v}_i(t) + \beta \sum_{i \in \mu} \vec{h}_i(\vec{r}_i, t) + \eta \vec{u}(t) \right], \quad (20)$$

where  $\alpha$ ,  $\beta$  and  $\eta$ , respectively, regulate the weights of the alignment with the peripheral particles velocity, the harmonic forces,  $\vec{h}_i$ , produced by peripheral particles on the central one, and the intensity of the unitary noise vector  $\vec{u}$ . The evolution equation for the peripheral particle  $i$  in cell  $\mu$  is similar

$$\vec{x}_i^\mu(t + \Delta t) = \vec{x}_i^\mu(t) + \vec{v}_i^\mu(t)\Delta t. \quad (21)$$

The interaction between peripheral particles of the same cell and particles of different cells ( $i$  and  $j$  in Fig. 8) results from the sum of several contributions. The particle  $i$  in cell  $\mu$  has velocity direction  $\theta$  given by

$$\theta_i^\mu = \arg [A_i^\mu + F_i^\mu + G_i^\mu + H_i^\mu + T_i^\mu], \quad (22)$$

where each term is explained one by one below.

First, consider a peripheral particle  $i$  that is part of the cell  $\mu$ . The total alignment acting on it,  $A_i^\mu$ , is composed of the central particle direction  $\hat{v}_\mu$ , that is a self-persistence term, and the direction of the velocity of neighboring peripheral particles either from cell  $\mu$  and from neighboring cells  $\nu$ :

$$A_i^\mu = \alpha \hat{v}^\mu + \alpha \sum_{i,j \in \mu} \hat{v}_{i,j}^{\mu,\mu} + \alpha_1 \sum_{i \in \mu, j \in \nu} \hat{v}_{i,j}^{\mu,\nu}. \quad (23)$$

The second term in Eq. (22) is a force term and also involves

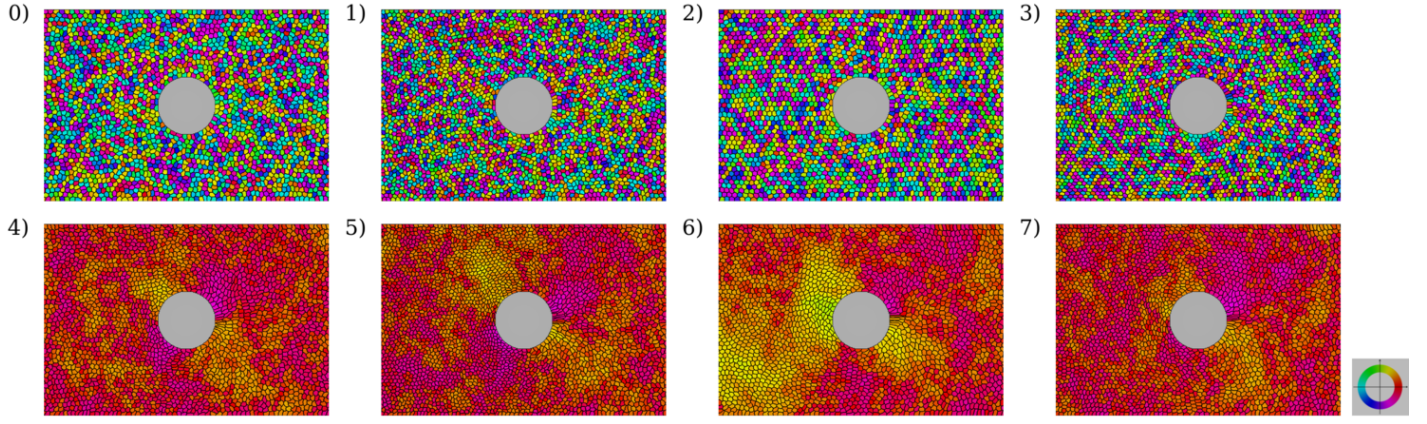


Fig. 7 Snapshots for the Potts model's eight limit cases; same caption as Fig. 4. See Table 7 for parameter values.

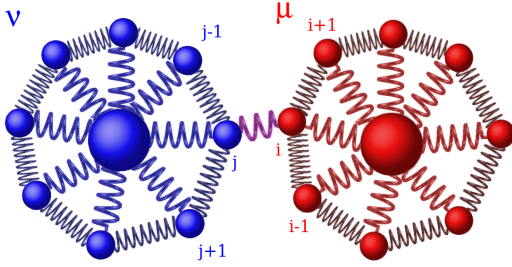


Fig. 8 Multiparticle model. Schema of the springs composing the extended cell model, including interaction with neighboring cells. Each cell and its central particle is labelled by a Greek letter, here  $\mu$  and  $\nu$ . The cells  $\mu$  and  $\nu$  interact only via their peripheral particles  $\mu, i$  and  $\nu, j$ .

contributions from the central particle and from peripheral particles,

$$F_i^\mu = \beta \left( \vec{h}_i^\mu + \sum_{j \sim i} \vec{h}_{i,j}^\mu \right) + \beta_1 \sum_{i \in \mu, j \in \nu} \vec{f}_{i,j}^{\mu,\nu} \quad (24)$$

where  $\vec{h}$  is an infinite range harmonic interaction between peripheral particles of the same cell or with the central particle of their cell. The last term represents interactions with peripheral particles of the same cell  $\mu$  when not first neighbors, or from a neighbor cell  $\nu$ . This last force between pairs is inspired by the force for Vicsek-like particles (Eq. 6): it is radial, with limited reach and its module depends on the distance  $r_{i,j}^{\mu,\nu}$  between peripheral particles

$$f(r_{i,j}^{\mu,\nu}) = \begin{cases} 0 & r_{i,j}^{\mu,\nu} \geq r_{\max} \\ 1 - \frac{r_{i,j}^{\mu,\nu}}{r_{\text{eq}}} & r_c < r_{i,j}^{\mu,\nu} < r_{\max} \\ f_c & r_{i,j}^{\mu,\nu} \leq r_c. \end{cases} \quad (25)$$

Here,  $r_{\max}$  is the cut-off, or maximum interaction distance,  $r_{\text{eq}}$  is the equilibrium distance,  $r_c$  is the core size, and  $f_c$  plays the role of an infinite repulsion force. In practice, in the simulation it is set to a large value compared to typical forces in the system.

The next force reflects the cell area constraint:

$$G_i^\mu = -k_A(A^\mu - A_0)\hat{r}_i^\mu, \quad (26)$$

where  $A^\mu$  is the instantaneous cell area,  $A_0$  is a target area,  $\hat{r}_i^\mu$  is a unitary radial vector and  $k_A$  is a stiffness constant.

The polygonal shape of each cell is not impenetrable: in principle a peripheral particle could invade another cell. In practice this seldom happens, but for these rare cases we introduce a force to repel the invader:

$$H_j^\mu = \begin{cases} f_c \hat{r}_i^{\mu,\nu} & \text{if } j \text{ inside } \mu \\ 0 & \text{else,} \end{cases} \quad (27)$$

with  $f_c$  and  $\hat{r}_i$  as defined above, and with an equal force with opposite sign that is applied to the center particle of cell  $\mu$ .

Since the topological relations between peripheral particles are fixed within a cell, we introduce a torque that keeps the particle near the correct relative angle with its neighbors. The tangential force resulting from this torque is given by

$$T_i^\mu = \kappa r_i^\mu \sum_{j=\pm 1} \phi_j^\mu - \phi_0, \quad (28)$$

where  $\phi_0$  is an equilibrium angle,  $r_i^\mu$  is the radial distance to the center particle,  $\phi_{i\pm 1}^\mu$  is the angle between peripheral particles  $i$  and  $i \pm 1$ , and  $\kappa$  is a constant.

In this work we keep constant all parameters (Table 9) except for three parameters we vary (Table 10).

The first parameter we vary is the external alignment  $\alpha_1$ , which we increase in order to establish collective movement.

The second parameter we vary is the attractive force between different cells  $\beta_1$ . If the attractive force  $\beta_1$  is low or even zero, particles from different cells still repel each other due to core repulsion. All forces are fixed at a value carefully chosen in order to prevent artifacts such as cell breakage, overlap or collapse.

The third parameter is the cell creation rate, which determines the density. As in the Potts model, the creation of new particles is implemented by cell division, which happens at a given rate,  $\tau$ .

Fig. 9 shows simulation snapshots in limit cases, see Table 11. Note the presence of voids and coherent polarization patches when

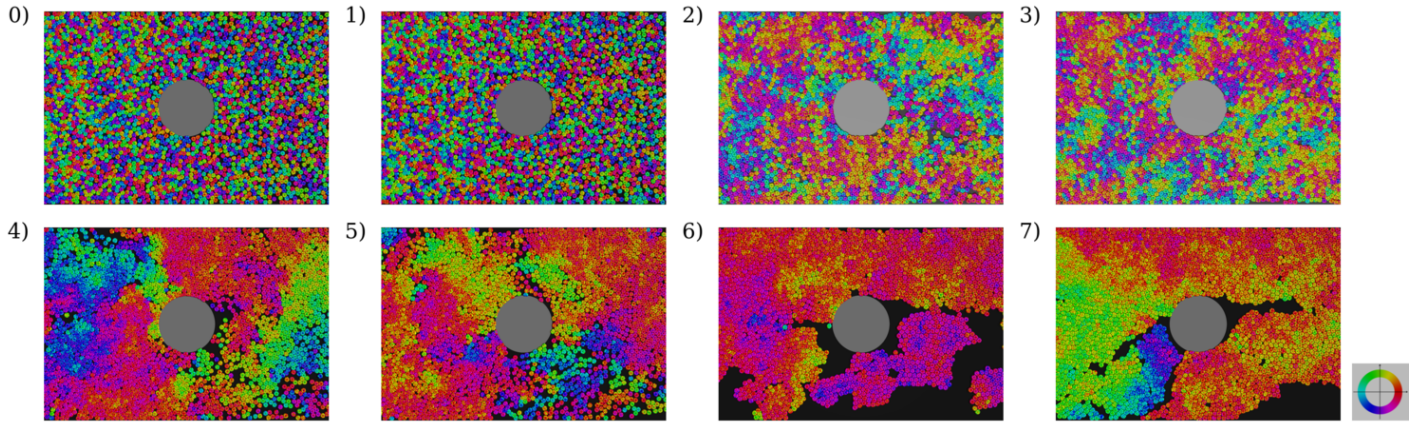


Fig. 9 Snapshots for the Multiparticle's eight limit cases; same caption as Fig. 4. See Table 10 for parameter values.

Parameter	Value
$N$	20
$\alpha$	14
$\beta$	1
$\eta$	1
$r_{eq}$	1.1
$r_{max}$	1.3
$k_a$	10
$\kappa$	10
$\phi_0$	$2\pi/N$
$R$	$N/(2\pi)$
$A_0$	$\pi R^2$

Table 9 Parameters kept constant in the Multiparticle model.  $N$  is the number of peripheral particles composing each cell.

Parameter	Level	Value
Alignment ( $\alpha_1$ )	low	0.0
Alignment ( $\alpha_1$ )	high	14.0
Force ( $\beta_1$ )	low	1.0
Force ( $\beta_1$ )	high	2.5
Creation ( $\tau$ )	low	50
Creation ( $\tau$ )	high	30

Table 10 Limit values for the parameters varied in the Multiparticle model.

the alignment is high and the motion is collective. Even with a high self-persistence value, collective alignment is never reached, probably because peripheral particles generate a lot of noise.

### 3 Results

Figs. 10-19 represent the output measurement maps for the five models, using the scheme explained above: In Figs. 10, 12, 14, 16, and 18, the normalized density  $\delta\rho$  is in color, with blue, white and red representing density lower, equal and higher than the equilibrium density  $\rho_{eq}$ , respectively. Velocity is represented as black arrows on the same plot, with a yellow unit scale arrow shown in the middle of the obstacle. When the flow is slow and disordered the scale appears large, while when a strongly collective flow is established the scale appears small. In Figs. 11, 13, 15, 17 and 19, the deformation anisotropy magnitude and direction are rep-

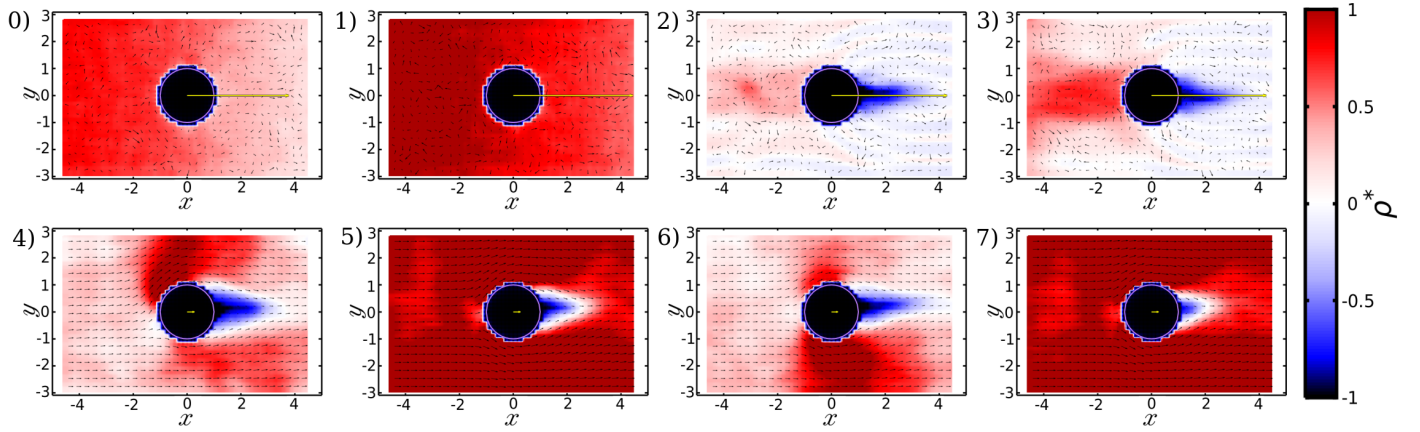
id	$\phi$	$\Delta$	$\delta\rho$
0	0.182	0.086	0.098
1	0.161	0.145	-0.013
2	0.285	0.337	-0.050
3	0.290	0.353	-0.010
4	0.643	0.439	-0.028
5	0.599	0.654	0.030
6	0.671	0.720	-0.240
7	0.794	0.708	-0.079

Table 11 Input measurements for the Multiparticle model. A lighter color means the simulation was performed with a lower level of the parameter related to that measure, a darker color means a higher level of that parameter, see Table 10.

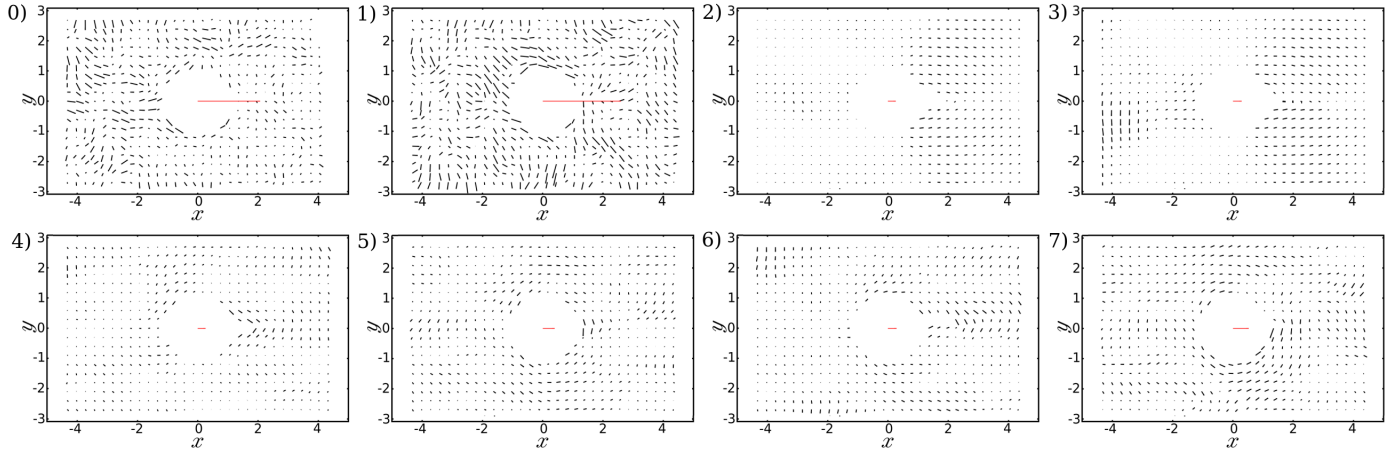
resented by a bar length and direction. To indicate the scale, the red line in the middle of the obstacle represents the deformation  $\ln 2$ , corresponding to cells whose length is twice their width. This means when the cell deformations are small and disordered, the scale appears large, while when a strongly collective deformation pattern is established the scale appears small.

Figure 10 presents velocity-density maps for the Vicsek model. At low alignment, the density is higher before the obstacle, and its distribution is symmetrical around the  $y$ -axis. In contrast, at high alignment and low densities (Figs. 10-4 and 10-6), there is a break in the density distribution symmetry, and the region of high density shifts towards one of the narrow spaces between the obstacle and the wall. The deformation maps (11) indicate an upstream/downstream asymmetry, particularly near the obstacle, where the direction close to it is favored. When compared to the other cases, the low alignment and low attraction cases (maps 0 and 1) exhibit minimal deformations.

Figures 12 and 13 illustrate the Szabo model's behavior. In all cases, the density map appears to be roughly symmetrical with respect to the  $y$ -axis, with high densities before the obstacle. The deformations observed in this model are more intense than those in the Vicsek model and display different patterns before the obstacle. When the alignment is low (maps 0-4), the deformation is primarily in the  $x$ -direction. In contrast, at high alignment, except for the high-density and low adhesion case (map 5), there is a



**Fig. 10** Vicsek model: density and velocity. The numbers in the image are the labels detailed in Table ?? . The values for the parameters used in this model are specified in Table 1. Images with even numbers present systems with density close to confluence, while the odd ones are constructed with higher densities. The top row presents the low alignment cases while the bottom one presents the high alignment ones. The four images on the left correspond to low forces (liquid-like), while the four images on the right correspond to high forces (solid-like). The images are restricted to an area around the obstacle; particle source and sink regions are not depicted.



**Fig. 11** Vicsek model: deformation anisotropy, for the same data as in Fig. 10.

region of low deformation just downstream of the obstacle. However, upstream of the obstacle, a region of high deformation can be observed.

The Voronoi model, as depicted in Figs. 14 and 15, exhibits significant density fluctuations with explicit alignment. Similar to the Vicsek model, low alignment results in small deformations, which increase significantly with both types of alignments. Additionally, deformations are closely tangential to the obstacle in most cases.

Figures 16 and 17 demonstrate the Potts model's behavior. With the exception of map 0, the density is higher before the obstacle, and some accumulation occurs close to the obstacle in case of low adhesion and high alignment (map 4). Furthermore, a clear contrast in the velocity field is evident in cases with and without alignment (maps 0,1,2,3 versus maps 4,5,6,7). The deformations are primarily tangential to the obstacle in the upstream and lateral parts of the obstacle. However, they are parameter-dependent in

the downstream part, as demonstrated by the comparison between maps 4 and 6 on one side and 3 and 5 on the other.

Within the parameter range investigated in this study, the Multiparticle model (Figs. 18, 19) exhibits coherent polarization waves but does not exhibit complete ordering. The density exhibits limited variation, and fluctuations arise due to averaging over void regions. Tangential deformation is dominant near the obstacle, although voids can alter this behavior.

## 4 Discussion: Choosing a model

For each given scientific question, several criteria can help to choose a suitable numerical model. In order to help the reader, we provide several comparison tables. Table 12 provides an overview of the physical ingredients incorporated in each model.

Table 13 explains how to choose the model parameter in order to avoid artifacts and execution troubles. For instance, some of the parameters only make sense for positive values, such as the align-

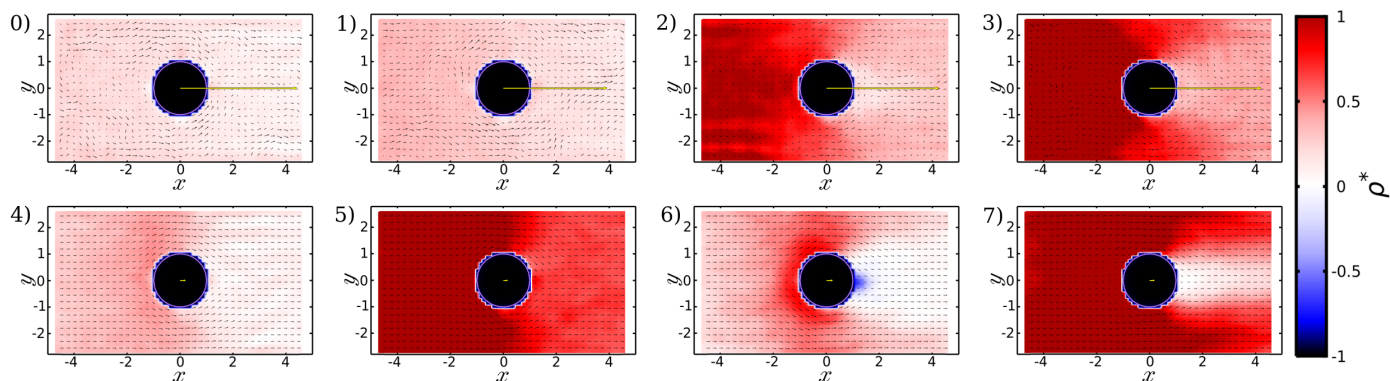


Fig. 12 Szabó model: density and velocity, for the 8 cases outlined in Tables 3 and 4.

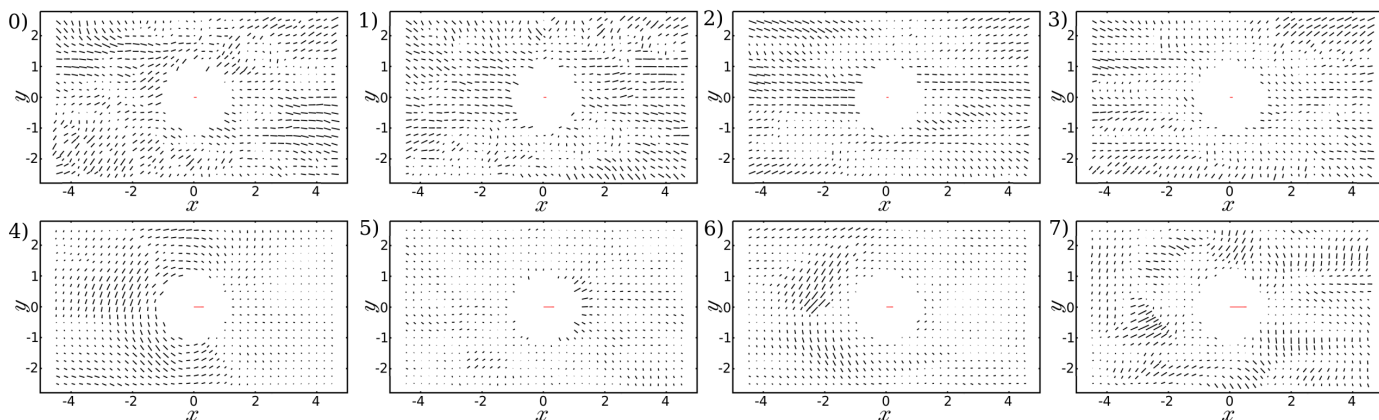


Fig. 13 Szabó model: deformation anisotropy, for the 8 cases outlined in Tables 3 and 4.

ment or the force between cells. In some cases, if the interaction or the junction tension is too strong, the cells can shrink or even disappear. In the Potts and Multiparticle models, cells may break if the alignment parameter is excessive.

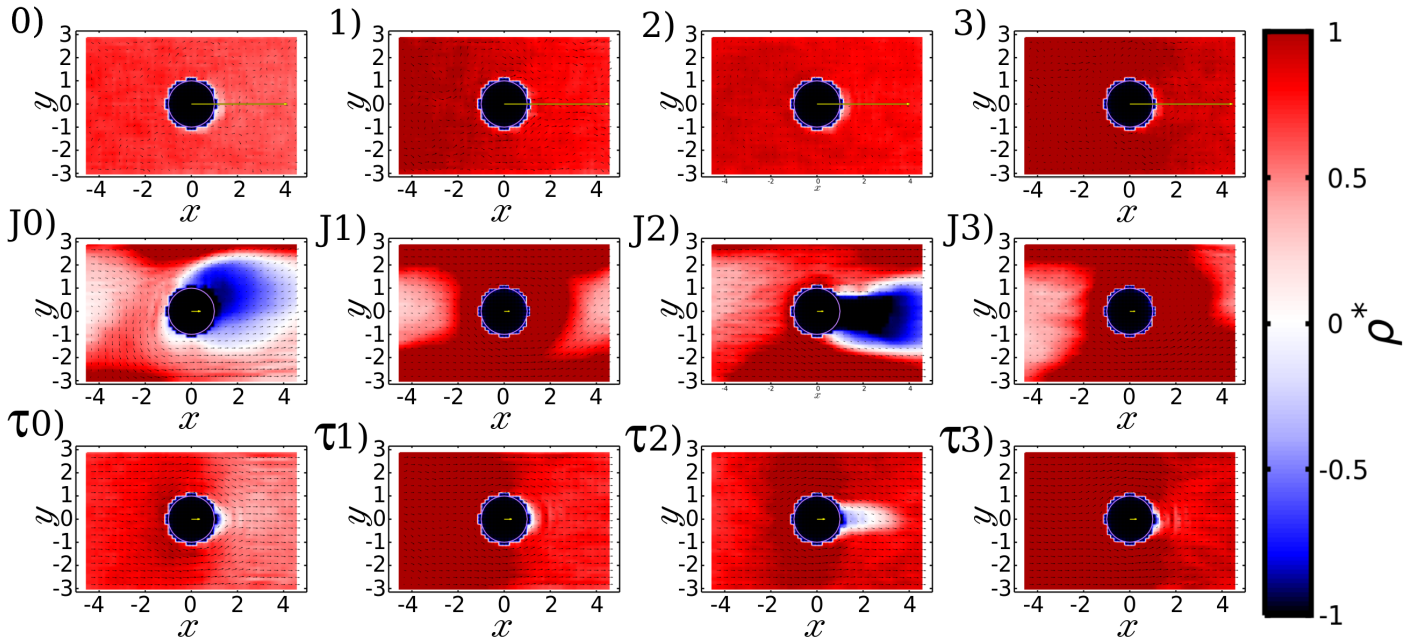
In all models the density should be carefully adjusted: In the Voronoi model, which is always confluent by construction (no free space is allowed), a too low density induces very unrealistic cell shapes and velocities. In the other models a too low density prevents confluence, i.e. some cells form small groups surrounded by free space. Conversely, at high density in all models except for Potts, the pressure becomes too high and induces spurious movements, cell overlaps or obstacle invasion. In particular, in the Multiparticle model cells easily overlap which induces severe artifacts.

Table 14 compares the range of input measurements range that each model can reasonably simulate. Since these input measurements are standardized and dimensionless, this comparison is physically relevant. For instance, all models enable us to vary alignment  $\phi$ , but the Vicsek model can produce high alignment, while the Potts and Multiparticle models are restricted to smaller values of  $\phi$  to remain stable. The Multiparticle model is suitable for low density simulations; in fact, density falls below the equilibrium one when in collective motion. In the other four models it is possible to increase the density above the equilibrium value by

controlling the cell creation rate. The Voronoi model is the most suitable for reaching a high density.

All models reasonably reproduce both liquid and solid behaviours, although this can be sensitive to alignment, to forces and to several artifacts. More precisely, in the absence of collective behavior (low  $\phi$ ), Vicsek, Szabó and Potts models present  $\Delta$  values which increase with the force. In collective motion (high  $\phi$ ), the Vicsek, Szabó and Potts models show solid behaviour (high  $\Delta$ ) independently of attraction forces or density. Conversely, the Voronoi model displays a liquid behavior (low  $\Delta$ ) at high densities, whatever the force; while in the Multiparticle model, at high force cell shapes become more irregular, neighbor exchanges become more frequent and thus the behaviour becomes liquid ( $\Delta$  decreases).

Finally, as expected, the Vicsek and Szabó models are simple and robust. Conversely, the Potts and Multiparticle models offer realistic shapes, shape changes and neighbour exchanges. In between, the Voronoi model is often a good compromise. Table 15 refines this comparison. These appreciations are entirely subjective and solely intended to help in choosing a suitable model. Criteria include the physical ingredients, parameter limitations, quantities to be measured, possible artifacts, simulation running time, and even the likelihood of execution crashes. For instance, depending on the flow alignment and spatial gradients, after the obstacle a hole



**Fig. 14** Voronoi model: density and velocity, for the 12 cases outlined in Tables 5 and 6. In J2, regions downstream of the obstacle with aberrant cell shapes and velocities have been removed.

	Vicsek	Szabó	Voronoi	Potts	Multiparticle
Degree of freedom	Particle	Particle	Particle	Contours	Multiparticle
Cell shape	Disk	Disk	Polygon	Set of pixels	Polygon
Alignment	Neighbor	Persistence	Both	Both	Both
Interaction	Force	Force	Tension	Tension	Force
Core	Hard	Soft	Soft	None	Hard
Lattice	No	No	No	Yes	No
Speed	Fixed	Variable	Variable	Variable	Fixed
Walls	Repulsive	Repulsive	Attractive	Attractive	Repulsive
Obstacle	Repulsive	Friction	Attractive	Attractive	Repulsive
Cell source	Creation	Creation	Division	Division	Division
Cell death	Yes	Yes	No	Yes	Yes

**Table 12** Overview of model ingredients. "Force" refers to pairwise radial forces between cell centers, while "tension" refers to cell-cell junction tension.

can appear (or, in the Voronoi model, cell shapes and velocities become unrealistic).

## 5 Conflicts of Interest

There are no conflicts of interest to declare.

## 6 Acknowledgments

This project has been funded by CAPES-COFECUB Ph 880-17 "From cell to tissue: collective mechanical behaviours". C.B. has been funded by CAPES and by ANR "Migrafolds". We thank M. Durand for critical reading of the manuscript. We thank S. Tlili for Fig. 1; and R. de Almeida, G. Thomas, M. Durande, S. Tlili, H. Delanoë-Ayari for discussions. We thank R. Sknepnek for his guidance in setting up the Voronoi simulation using SAMoS<sup>54</sup>. We dedicate this work to the memory of C. Kirch.

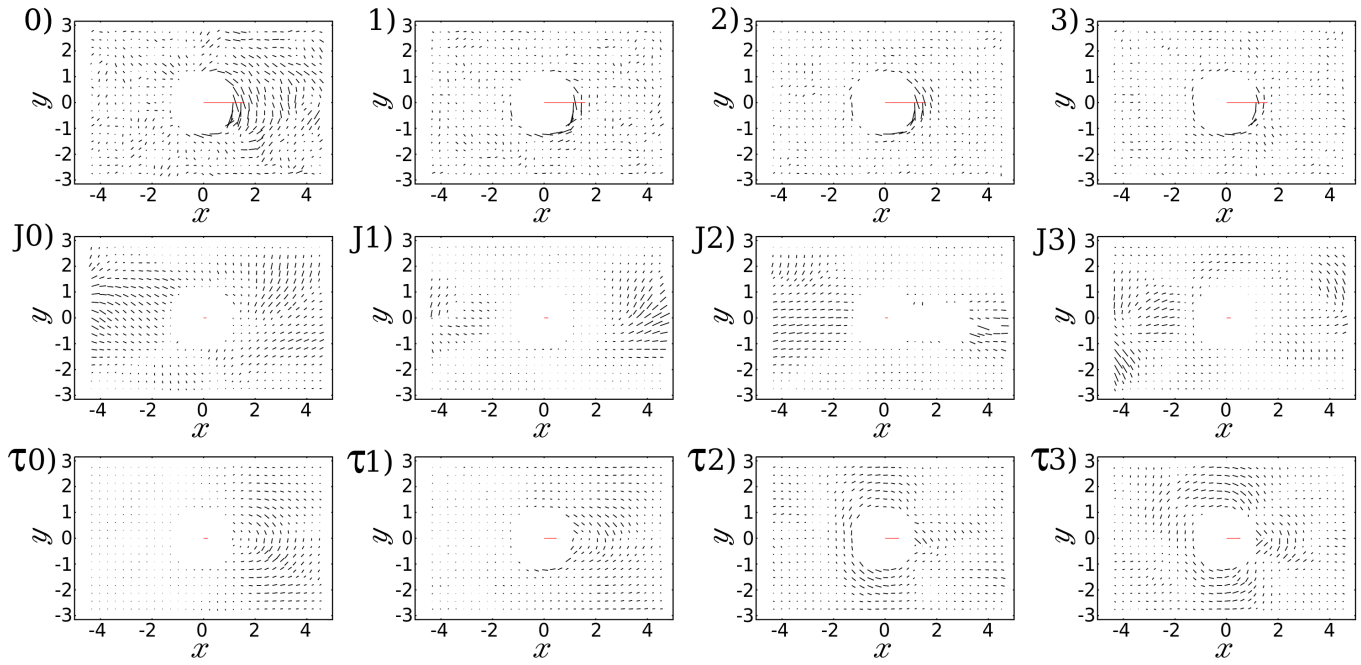


Fig. 15 Pictures/Voronoi model: deformation anisotropy, for the 12 cases outlined in Tables 5 and 6. In J2, regions downstream of the obstacle with aberrant cell shapes and velocities have been removed.

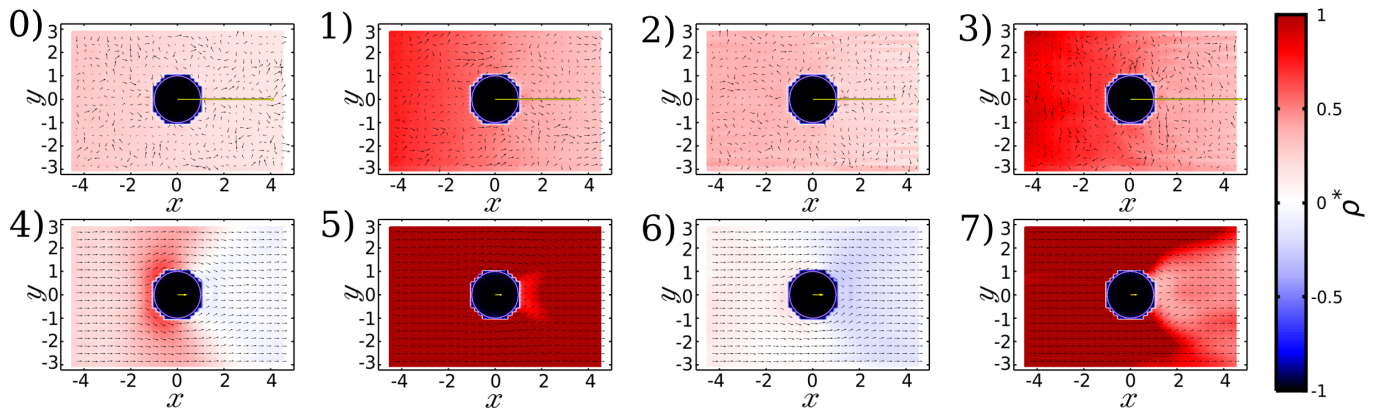


Fig. 16 Potts model: density and velocity, for the 8 cases outlined in Tables 7 and 8.



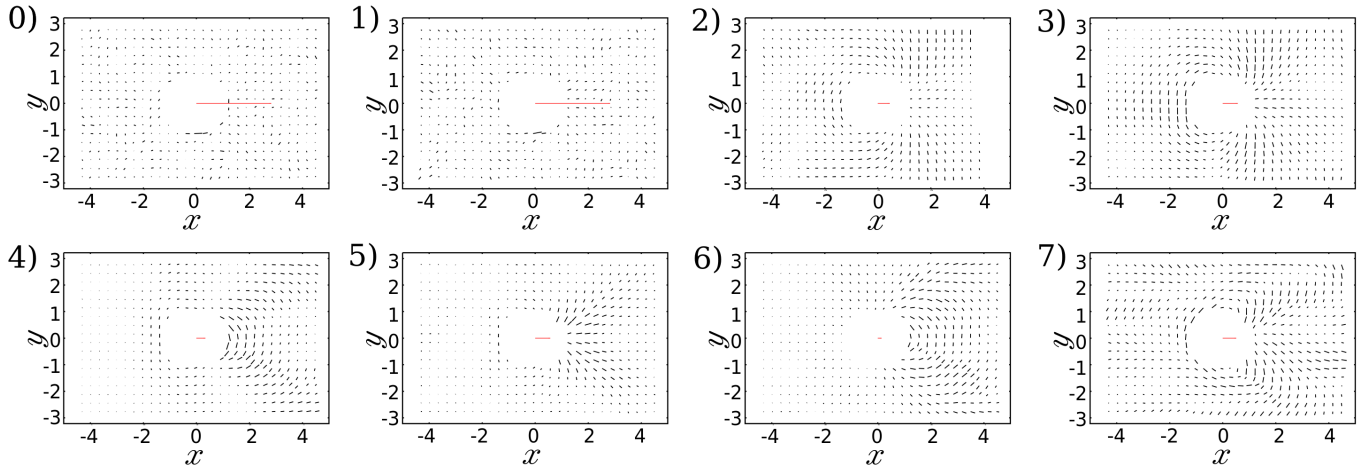


Fig. 17 Potts model: deformation anisotropy, for the 8 cases outlined in Tables 7 and 8.

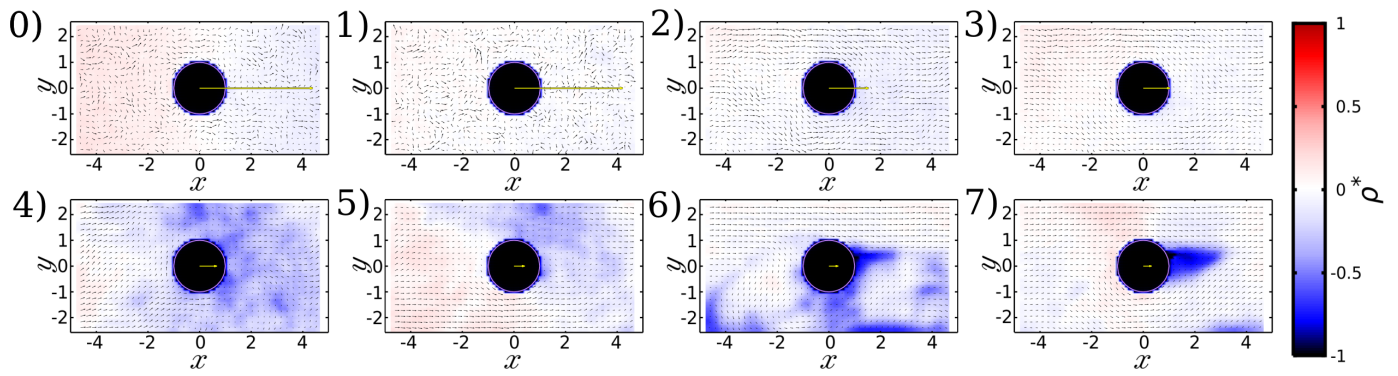


Fig. 18 Multiparticle model: density and velocity, for the 8 cases outlined in Tables 10 and 11.

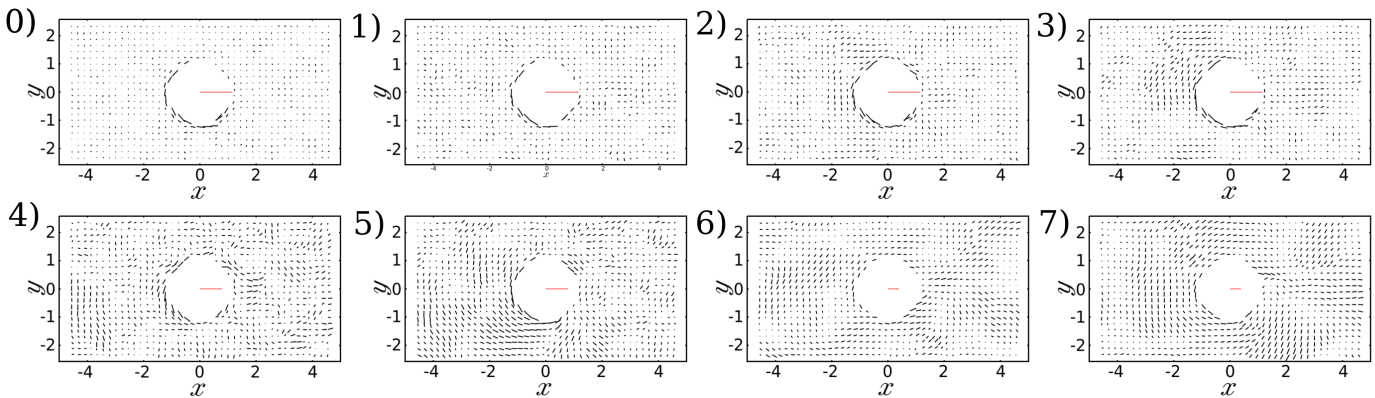


Fig. 19 Multiparticle model: deformation anisotropy, for the 8 cases outlined in Tables 10 and 11.

	Vicsek	Szabó	Voronoi	Potts	Multiparticle
Lowest alignment	0.0 <i>disorder</i>	N/A	0.0 <i>disorder</i>	0.0 <i>disorder</i>	0.0 <i>disorder</i>
Highest alignment	no limit	N/A	finite <i>alignment drops</i>	finite <i>cells break</i>	finite <i>cells break</i>
Lowest persistence	N/A	$1/\tau \rightarrow 0$ <i>disorder</i>	$1/\tau \rightarrow 0$ <i>disorder</i>	0.0 <i>disorder</i>	0.0 <i>disorder</i>
Highest persistence	N/A	finite <i>alignment drops</i>	finite <i>tissue collapse</i>	finite <i>cells break</i>	finite <i>cells break</i>
Lowest interaction	finite <i>gas</i>	finite <i>gas</i>	finite <i>rosettes</i>	finite <i>cells break</i>	finite <i>gas</i>
Highest interaction	core repulsion <i>cores overlap</i>	repulsion force <i>cores overlap</i>	finite <i>cells collapse</i>	finite <i>cells collapse</i>	finite <i>cells break</i>
Lowest density	confluence <i>holes</i>	confluence <i>holes</i>	confluence <i>retraction</i>	confluence <i>holes</i>	confluence <i>holes</i>
Highest density	finite <i>cores overlap, invade obstacle</i>	finite <i>cores overlap</i>	finite <i>cells are liquid, execution crashes</i>	finite <i>cells collapse</i>	finite <i>cells collapse and/or overlap</i>

**Table 13** Model parameter limitations. For each model, lower and upper limits are suggested in the top line. For each limit, a reason for this choice (e.g. the appearance of an artifact) is indicated in *italics* in the bottom line. Here we use N/A: not applicable.

	Vicsek	Szabó	Voronoi	Potts	Multiparticle
Alignment					
low $\phi$	0.12	0.2	0.17	0.09	0.2
high $\phi$	0.98	0.9	0.9	0.5	0.6
Density					
low $\delta\rho$	0.05	0.2	0.5	0.25	-0.1
high $\delta\rho$	1.0	1.0	1.1	1.1	0.1
Liquid / solid					
low $\Delta$	0.02	0.2	0.2	0.09	0.1
high $\Delta$	0.85	0.85	0.7	0.8	0.7

**Table 14** Input measurements range reached for each model. All values indicated are approximate. Remember that the normalized density is compared with the equilibrium density (Eq. 3), hence can reach negative values.

	Vicsek	Szabó	Voronoi	Potts	Multiparticle
Density range	★★★★★	★★★★★	★★★☆☆	★★★★☆	★★☆☆☆
Density fluctuations	★★★★★	★★★☆☆	★★★★☆	★★★★☆	★★☆☆☆
Tissue shrinkage	★★☆☆☆	★★★☆☆	★★★★★	★★★★☆	★★☆☆☆
Cell shape	★★★☆☆	★★★☆☆	★★★★☆	★★★★★	★★★★★
Cell stretch	★★☆☆☆	★★☆☆☆	★★★★★	★★★☆☆	★★★★☆
Cell velocity	★★★☆☆	★★★☆☆	★★★★☆	★★★☆☆	★★☆☆☆
Velocity asymmetry	★★★☆☆	★★★☆☆	★★★★★	★★★☆☆	★★☆☆☆
Cell self-persistence	☆☆☆☆☆	★★★★☆	★★★★★	★★★★☆	★★★★☆
Neighbour alignment	★★★★★	★★★★☆	★★★★☆	★★★☆☆	★★★★☆
Neighbour exchange	★★★☆☆	★★★☆☆	★★★★☆	★★★★★	★★★★☆
Closing after obstacle	★★☆☆☆	★★★☆☆	★★☆☆☆	★★★★★	★★★★☆
Simulation time efficiency	★★★★★	★★★★★	★★★☆☆	★★☆☆☆	★★☆☆☆
Simulation stability	★★★★☆	★★★★☆	★★☆☆☆	★★★★☆	★★★★☆
Number of cells	~ 7600	~ 11400	~ 8100	~ 7500	~ 7300
Main advantages	robustness, simplicity	simplicity, alignment	good compromise	shape, fluctuations	large deformations
Main limitation	shape	shape	density	alignment	density

**Table 15** Model guide chart: subjective appreciations of each model's advantages (5 colored stars indicate the best quality).

## Notes and references

- 1 S. R. K. Vedula, A. Ravasio, C. T. Lim and B. Ladoux, *Physiology*, 2013, **28**, 370–379.
- 2 J. Stock and A. Pauli, *Development*, 2021, **148**, dev191767.
- 3 P. Friedl, *Curr. Opin. Cell Biol.*, 2004, **16**, 14–23.
- 4 R. Etournay, M. Popovic, M. Merkel, A. Nandi, C. Blasse, B. Aigouy, H. Brandl, G. Myers, G. Salbreux, F. Jülicher and S. Eaton, *eLife*, 2015, **4**, e07090.
- 5 B. Guirao, S. U. Rigaud, F. Bosveld, A. Bailles, J. López-Gay, S. Ishihara, K. Sugimura, F. Graner and Y. Bellaïche, *Elife*, 2015, **4**, e08519.
- 6 J. B. Green, *Development*, 2022, **149**, dev199794.
- 7 S. Tlili, M. Durande, C. Gay, B. Ladoux, F. Graner and H. Delanoë-Ayari, *Phys. Rev. Lett.*, 2020, **125**, 088102/1–6.
- 8 I. Pajic-Lijakovic and E. H. Barriga, *Viscoelasticity and Collective Cell Migration. An interdisciplinary perspective across levels of organization*, Academic Press, 2021.
- 9 D. Bi, X. Yang, M. C. Marchetti and M. L. Manning, *Phys. Rev. X.*, 2016, **6**, 021011.
- 10 A. Hopkins, M. Chiang, B. Loewe, D. Marenduzzo and M. C. Marchetti, *Phys. Rev. Lett.*, 2022, **129**, 148101.
- 11 T. Vicsek, A. Czirók, E. Ben-Jacob, I. Cohen and O. Shochet, *Phys. Rev. Lett.*, 1995, **75**, 1226–1229.
- 12 G. Grégoire, H. Chaté and Y. Tu, *Physica D: Nonlinear Phenomena*, 2003, **181**, 157 – 170.
- 13 S. Ramaswamy, *Ann. Rev. Cond. Matt. Phys.*, 2010, **1**, 323–345.
- 14 M. C. Marchetti, J.-F. Joanny, S. Ramaswamy, T. B. Liverpool, J. Prost, M. Rao and R. A. Simha, *Rev. Mod. Phys.*, 2013, **85**, 1143.
- 15 S. Huang, C. P. Brangwynne, K. K. Parker and D. E. Ingber, *Cell Motil. Cytosk.*, 2005, **61**, 201–213.
- 16 S. J. Streichan, G. Valentin, D. Gilmour and L. Hufnagel, *Phys. Biol.*, 2011, **8**, 045004.
- 17 G. Weber, M. Bjerke and D. D.W., *Dev. Cell.*, 2012, **22**, 104–115.
- 18 M. Paoluzzi, D. Levis and I. Pagonabarraga, *Comm. Phys.*, 2022, **5**, 111.
- 19 S. Tlili, E. Gauquelin, B. Li, O. Cardoso, B. Ladoux, H. Delanoë-Ayari and F. Graner, *R. Soc. Open Sci.*, 2018, **5**, 172421.
- 20 F. J. Segerer, F. Thüroff, A. P. Alberola, E. Frey and J. O. Rädler, *Phys. Rev. Lett.*, 2015, **114**, 228102.
- 21 P. J. Albert and U. S. Schwarz, *PLoS Comput. Biol.*, 2016, **12**, e1004863.
- 22 A. Buttenschön and L. Edelstein-Keshet, *PLoS Comput. Biol.*, 2020, **16**, e1008411.
- 23 B. Szabó, G. Szöllösi, B. Gönci, Z. Jurányi, D. Selmeczi and T. Vicsek, *Phys. Rev. E*, 2006, **74**, 061908.
- 24 N. Sepúlveda, L. Petitjean, O. Cochet, E. Grasland-Mongrain, P. Silberzan and V. Hakim, *PLoS Comput. Biol.*, 2013, **9**, e1002944.
- 25 S. Hoehme and D. Drasdo, *Bioinformatics*, 2010, **26**, 2641–2642.
- 26 F. Frascoli, B. Hughes, M. Zaman and K. Landman, *PLoS One*, 2013, **8**, e59249.
- 27 I. Montenegro-Rojas, G. Yañez, E. Skog, O. Guerrero-Calvo, M. Andaur-Lobos, L. Dolfi, A. Cellerino, M. Cerda, M. L. Concha, C. Bertocchi, N. O. Rojas, A. Ravasio and T. J. Rudge, *Front. Cell Dev. Biol.*, 2023, **11**, 959611.
- 28 D. Barton, S. Henkes, C. Weijer and R. Sknepnek, *PLoS Comput. Biol.*, 2017, **13**, e1005569.
- 29 S. Tlili, J. Yin, J.-F. Rupperecht, M. A. Mendieta-Serrano, G. Weissbart, N. Verma, X. Teng, Y. Toyama, J. Prost and T. E. Saunders, *Proc. Natl. Acad. Sci. U. S. A.*, 2019, **116**, 25430–25439.
- 30 F. Pérez-Verdugo, J.-F. Joanny and R. Soto, *Phys. Rev. E*, 2020, **102**, 052604.
- 31 J. Käfer, P. Hogeweg and A. F. M. Marée, *PLOS Computational Biology*, 2006, **2**, 1–12.
- 32 A. J. Kabla, *J. R. Soc. Interface*, 2012, **9**, 3268–3278.
- 33 N. Guisoni, K. Mazzitello and L. Diambra, *Front. Phys.*, 2018, **6**, 61.
- 34 E. F. Teixeira, H. C. M. Fernandes and L. G. Brunnet, *Soft Matt.*, 2021, **17**, 5991–6000.
- 35 B. Loewe, M. Chiang and a. M. C. M. D. Marenduzzo, *Phys. Rev. Lett.*, 2020, **125**, 038003.
- 36 L. Ophaus, S. V. Gurevich and U. Thiele, *Phys. Rev. E*, 2018, **98**, 022608.
- 37 J. M. Osborne, A. G. Fletcher, J. M. Pitt-Francis, P. K. Maini and D. J. Gavaghan, *PLOS Comput. Biol.*, 2017, **13**, 1–34.
- 38 A. Fletcher, F. Cooper and R. Baker, *Philos. Trans. Roy. Soc. B: Biological Sciences*, 2017, **372**, 1720.
- 39 A. Fletcher and J. Osborne, *WIREs Mech. Dis.*, 2021, **14**, e1527.
- 40 G. G. Stokes, *Cambr. Philos. Soc. Trans.*, 1851, **9**, 8–106.
- 41 I. Cheddadi, P. Saramito, B. Dollet, C. Raufaste and F. Graner, *Eur. Phys. J. E*, 2011, **34**, 1.

- 42 J. H. Kim, X. Serra-Picamal, D. T. Tambe, E. H. Zhou, C. Y. Park, M. Sadati, J.-A. Park, R. Krishnan, B. Gweon, E. Millet, J. P. Butler, X. Trepast and J. J. Fredberg, *Nat. Mater.*, 2013, **12**, 856–863.
- 43 M. Durande, *Migration cellulaire par forçage d'hétérogénéité*, PhD thesis, Université de Paris, France, 2020.
- 44 P. Bardet, B. Guirao, C. Paoletti, F. Serman, V. Léopold, F. Bosveld, Y. Goya, V. Mirouse, F. Graner and Y. Bellaïche, *Dev. Cell*, 2013, **5**, 534 – 546.
- 45 S. Henkes, K. Kostanjevec, J. M. Collinson, R. Sknepnek and E. Bertin, *Nat. Comm.*, 2020, **11**, 1405.
- 46 J. M. Belmonte, G. L. Thomas, L. G. Brunnet, R. M. C. de Almeida and H. Chaté, *Phys. Rev. Lett.*, 2008, **100**, 248702.
- 47 T. Liu, X. Liu, D. Spring and et al., *Sci. Rep.*, 2014, **81**, 5418.
- 48 Y. Liu, T. Zhang, H. Zhang, J. Li, N. Zhou, R. Fiskesund, J. Chen, J. Lv, J. Ma, H. Zhang, K. Tang, F. Cheng, Y. Zhou, X. Zhang, N. Wang and B. Huang, *Cancer Res.*, 2021, **81**, 476–488.
- 49 J. Lv, Y. Liu, F. Cheng, J. Li, Y. Zhou, T. Zhang, N. Zhou, C. Li, Z. Wang, L. Ma, M. Liu, Q. Zhu, X. Liu, K. Tang, J. Ma, H. Zhang, J. Xie, Y. Fang, H. Zhang, N. Wang, Y. Liu and B. Huang, *EMBO J.*, 2020, **40**, e106123.
- 50 F. Graner, B. Dollet, C. Raufaste and P. Marmottant, *Eur. Phys. J. E*, 2008, **25**, 349–369.
- 51 M. Durande, S. Tlili, T. Homan, B. Guirao, F. Graner and H. Delanoë-Ayari, *Phys. Rev. E*, 2019, **99**, 062401.
- 52 S. Henkes, Y. Fily and M. C. Marchetti, *Phys. Rev. E*, 2011, **84**, 040301.
- 53 P. Baconnier, D. Shohat, C. Hernández-López, C. Coulais, V. Démary, G. Düring and O. Dauchot, *Nat. Phys.*, 2022, **18**, 1234–1239.
- 54 R. Sknepnek and et al, *Soft Active Matter on Surfaces (SAMoS)*, 2020, <https://github.com/sknepneklab/SAMoS>.
- 55 C. Malinverno, S. Corallino, F. Giavazzi, M. Bergert, Q. Li, M. Leoni, A. Disanza, E. Frittoli, A. Oldani, E. Martini et al., *Nat. Mater.*, 2017, **16**, 587–596.
- 56 F. Giavazzi, M. Paoluzzi, M. Macchi, D. Bi, G. Scita, M. L. Manning, R. Cerbino and M. C. Marchetti, *Soft matt.*, 2018, **14**, 3471–3477.
- 57 F. Graner and J. A. Glazier, *Phys. Rev. Lett.*, 1992, **69**, 2013–2016.
- 58 J. Glazier and F. Graner, *Phys. Rev. E*, 1993, **47**, 2128.
- 59 T. Hirashima, E. G. Rens and R. M. H. Merks, *Develop. Growth Differ.*, 2017, **59**, 329–339.
- 60 J. D. Treado, D. Wang, A. Boromand, M. P. Murrell, M. D. Shattuck and C. S. O'Hern, *Phys. Rev. Materials*, 2021, **5**, 055605.